universität wien

MASTERARBEIT | MASTER'S THESIS

Titel | Title

High-Frequency Antennas for All-Electrical Excitation and Detection of Propagating Spin Waves

verfasst von | submitted by

Andreas Höfinger BSc

angestrebter akademischer Grad | in partial fulfilment of the requirements for the degree of

Master of Science (MSc)

Wien | Vienna, 2024

Studienkennzahl lt. Studienblatt | Degree programme code as it appears on the student record sheet:	UA 066 876
Studienrichtung lt. Studienblatt | Degree programme as it appears on the student record sheet:	Masterstudium Physics
Betreut von | Supervisor:	Univ.-Prof. Dr. habil. Andrii Chumak
Mitbetreut von | Co-Supervisor:	Sebastian Knauer B.Sc. M.Sc. PhD

Acknowledgements

First and foremost I want to express my sincere gratitude to Dr. Sebastian Knauer for his tireless support and invaluable guidance throughout the course of my research. His mentorship and close supervision not only enhanced my knowledge in cleanroom procedures and experimental techniques but also significantly enriched my skills in scientific and academic writing and presentions. I also want to thank Prof. Andrii Chumak for his supervision of my master's thesis, and the opportunity to work as a student assistant during my studies. I am profoundly grateful for the trust and patience of Dr. Knauer and Prof. Chumak to let me work inedependently in the cleanroom facilities at the Central European Institue of Technology (CEITEC) in Czech Republic, Brno, which gave me the opportunity to fabricate my own nano-scale structures and gain the experience of working in a state-of-the-art research facility. Next, I want to emphasise my gratitude to my colleagues and friends David Schmoll, Andrey Voronov, Sebastian Lamb-Camarena, Pedro del Real Lavergne, Sabri Koraltan, Claas Abert, Kristýna Davídková, Khrystyna Levchenko, Noura Zenbaa, Barbora Budinská, Rostyslav Serha and Fabian Majcen. Without their innumerable support this work would not have been possible.

As well, I owe special thanks to the Central European Institue of Technology (CEITEC) for the possibility to use their clean room facilities and machines.

Beyond all, I devote my deep gratefulness to my friends and family, for supporting me during my whole academic education. I would like to thank Christian and Florian in particular for the countless memorable evenings filled with fruitful discussions, always willing to lend me their ear.

Especially, I thank my girlfriend Sophie, for always knowing the exact right ratio between supporting and pushing me during this extensive work.

Abstract

Accessing individual qubits as a quantum technology platform for novel computing capabilities and quantum hybrid systems has attracted growing scientific interest in the last decade. The novel field of quantum magnonics harnesses the potential of spin waves (SW) and their single quanta, magnons, to transmit, store, and process information in magnetically ordered materials [1–3]. The most widely used material for magnonic applications is monocrystalline yttrium iron garnet (YIG), typically grown on gadolinium gallium garnet (GGG) [4]. To probe the physics of these magnonic devices at sub-micrometre level, high-frequency compatible microwave-magnetic circuits for excitation and detection of spin waves are required.

Microantennas have already been utilised to excite spin waves with continuous or pulsed radio-frequency (RF) signals [5], leading to the demonstration of integrated magnonic circuits [6,7] and the control of Bose-Einstein condensates [8]. Propagating spin waves have shown a promising capability for novel quantum information processing applications [9, 10]. Hence, for the efficient coupling and detection of propagating magnons excited by RF-signals, large-area impedance-matched on-chip lithographed antennas are required [11–17]. Thus, the scientific objective of this thesis is to perform analytical and numerical calculations of the spin-wave excitation efficiency for micrometre-scale on-chip microwave antennas of different designs, to fabricate selected designs, and to compare the spin-wave excitation of the fabricated antennas experimentally.

First, I compared different antenna designs for low-loss and efficient spin-wave excitation, comprising literature study, analytical calculations, and multi-physics software simulations. The electromagnetic finite element simulations, performed using the software package *COMSOL Multiphysics*, were combined with micromagnetic finite difference numerical calculations using the python package *Magnum.np* and were compared with calculations conducted by the micromagnetic modelling package *TetraX*. I successfully transferred the magnetic field components obtained by the finite element electromagnetic simulation into a finite difference grid, which already forms the simulation box for the micromagnetic simulation including the exact shape of the magnetic field. Therefore, the numerical simulation includes the complete treatment of the problem, from the excitation of the RF signal in the antenna to the propagating spin wave.

I fabricated four different antenna pairs to optimize spin-wave excitation on 48 nm thick YIG using electron-beam lithography combined with physical vapour deposition at the Central European Institute of Technology (CEITEC, Brno, Czech Republic). The receiving and detecting antennas were consistently spaced 20 µm apart. The project was concluded by measuring the spin-wave excitation and detection experimentally at room temperature, using the antennas that were designed. To measure the spin-wave excitation and detection efficiency, I performed all-electrical propagating spin-wave spectroscopy (AEPSWS) up to 250 mT external field. The results were then compared between the different antenna designs and were checked for agreement with numerical and theoretical calculations.

In this study, I utilised a combination of the finite element electromagnetic and finite difference micromagnetic simulations of sub-micrometre antennas for SW excitation and detection. This work offers a new method to analyse different antenna structures in a complete treatment of the problem, from the excitation of an RF signal in the antenna to the propagating spin wave, which has not been demonstrated until now. The simulations results show good agreement with those obtained by measuring the fabricated antennas using all-electrical propagating spin-wave spectroscopy.

Kurzfassung

Der Zugriff auf einzelne Qubits als Quantentechnologieplattform für neuartige Rechenkapazitäten und Quanten-Hybridsysteme hat im letzten Jahrzehnt zunehmendes wissenschaftliches Interesse geweckt. Das neue Feld der Quantenmagnonik nutzt das Potenzial von Spinwellen und ihren zugehörigen Quantenteilchen, den Magnonen, um Informationen in magnetisch geordneten Materialien zu übertragen, zu speichern und zu verarbeiten [1–3]. Das am häufigsten verwendete Material für magnonische Anwendungen ist monokristalliner Yttrium-Eisen-Granat (YIG), der in der Regel auf Gadolinium-Gallium-Granat (GGG) gezüchtet wird [4]. Um die Physik dieser magnonischen Bauelemente im Submikrometerbereich zu untersuchen, sind hochfrequenzkompatible mikrowellenmagnetische Schaltkreise zur Anregung und zur Detektion von Spinwellen erforderlich.

Mikroantennen wurden bereits eingesetzt, um Spinwellen mit kontinuierlichen oder gepulsten Hochfrequenzsignalen anzuregen [5], was zur Demonstration integrierter magnonischer Schaltkreise [6, 7] und zur Erzeugung von Bose-Einstein-Kondensaten [8] führte. Die Ausbreitung von Spinwellen hat sich als vielversprechend für neuartige Anwendungen der Quanteninformationsverarbeitung erwiesen [9, 10]. Für die effiziente Kopplung und Detektion von sich ausbreitenden Magnonen, die durch HF-Signale angeregt werden, sind daher auf einem Chip lithografierte, großflächig impedanzangepasste Antennen erforderlich [11–17].

Das wissenschaftliche Ziel dieser Arbeit ist es daher, analytische und numerische Berechnungen der Spin-Wellen-Anregungseffizienz von On-Chip-Mikrowellenantennen unterschiedlichen Entwürfe im Mikrometerbereich durchzuführen, ausgewählte Entwürfe herzustellen und die Spin-Wellen-Anregung der hergestellten Antennen experimentell zu vergleichen.

Zunächst habe ich verschiedene Antennenentwürfe für eine verlustarme und effiziente Spinwellenanregung verglichen, die eine Literaturstudie, analytische Berechnungen und multiphysikalische Simulationen umfasst hat. Die elektromagnetischen Finite-Elemente-Simulationen, die mit dem Softwarepaket *COMSOL Multiphysics* durchgeführt wurden, wurden mit mikromagnetischen numerischen Finite-Differenzen-Berechnungen unter Verwendung des Python-Pakets *Magnum.np* kombiniert und mit Berechnungen verglichen, die mit dem mikromagnetischen Modellierungspaket *TetraX* durchgeführt wurden. Es ist mir gelungen, die durch die elektromagnetische Finite-Elemente-Simulation erhaltenen Magnetfeldkomponenten in ein Finite-Differenzen-Gitter zu übertragen, das die Simulationsbox für die mikromagnetische Simulation bildet und bereits die genaue Form des Magnetfelds enthält. Die numerische Simulation umfasst daher die vollständige Behandlung des Problems, von der Anregung des HF-Signals in der Antenne bis zur Ausbreitung der Spinwelle.

Zusätzlich habe ich vier verschiedene Antennen für eine optimale Spinwellenanregung mittels Elektronenstrahllithographie in Kombination mit physikalischer Gasphasenabscheidung am Central European Institute of Technology (CEITEC, Brno, Tschechische Republik) hergestellt. Die Antennen wurden auf 48 nm dickem YIG, das auf 500 µm GGG gezüchtet ist, fabriziert. Die Empfangs- und Detektionsantennen waren jeweils 20 µm voneinander entfernt.

Abgeschlossen habe ich das Projekt, indem ich die Anregung und die Detektion von Spinwellen bei Raumtemperatur unter Verwendung der hergestellten Antennenstrukturen gemessen habe. Zur Quantifizierung der Anregungs- und Detektionseffizienz habe ich eine voll-elektrische propagierende Spinwellenspektroskopie mit einem kalibrierten 20 GHz Vektornetzwerkanalysator (VNA) in Kombination mit einem Elektromagneten bei Feldern bis zu 250 mT durchgeführt. Die Ergebnisse der verschiedenen Antennenentwürfe wurden anschließend untersucht und mit den numerischen und theoretischen Berechnungen verglichen.

In dieser Arbeit habe ich eine umfassende Untersuchung von nanometer großen Hochfrequenz-On-Chip-Antennen für die vollelektrische Spektroskropie propagierender Spinwellen demonstriert.

Die verwendeten Methoden zeigen eine gute Übereinstimmung zwischen den durch Simulationen und Messungen erhaltenen Ergebnissen in Bezug auf die Spinwellen-Anregungsspektren der untersuchten Mikrowellenantennen. Diese Arbeit wird dazu beitragen, solche Antennen für die Realisierung integrierter Quantenmagnonik weiter zu optimieren und zu entwerfen.

Contents

List of Abbreviations

PSW	Propagating Spin Wave
LLG	Landau-Lifschitz-Gilbert
MSW	Magnetostatic Spin Wave
FVMSW	Forward Volume Magnetostatic Spin Wave
BVMSW	Backward Volume Magnetostatic Spin Wave
MSSW	Magnetostatic Surface Spin Wave
YIG	Yttrium Iron Garnet
EM	Electromagnetic
RF	Radio Frequency
AC	Alternating Current
GGG	Gadolinium Gallium Garnet
CPW	Coplanar Waveguide
AEPSWS	All Electrical Propagating Spin Wave Spectroscopy
FFT	Fast Fourier Transformation
EBL	Electron Beam Lithography
PMMA	Polymethylmethacrylate
SEM	Scanning Electron Microscope
VNA	Vector Network Analyser

1 Theoretical background

To understand and interpret the physical phenomena investigated during this work I review the theoretical context in this chapter.

In Section 1.1 fundamentals of magnetism are addressed. Section 1.2 introduces dynamics of magnetisation, leading to the introduction of spin waves in thin films in Section 1.3 and 1.4. The material of choice for magnetic dynamics is discussed in Section 1.5. After an introduction to microwave engineering in Section 1.6 an explanation of spin-wave transducers is covered in Section 1.7.

1.1 Magnetism

In a semi-classical view, an atom's magnetic dipole moment $\mathbf{m}$ mainly comes from the electrons' spin magnetic moment $\boldsymbol{\mu}_s$ and its orbital magnetic moment $\boldsymbol{\mu}_\mathrm{e}$, which is related to its orbital angular momentum $\mathbf{L}_\mathrm{e}$ by

$$\boldsymbol{\mu}_\mathrm{e} = -\gamma\, \mathbf{L}_\mathrm{e}, \tag{1}$$

with

$$\gamma = -g\frac{q}{2m_\mathrm{e}} \tag{2}$$

the gyromagnetic ratio for an isolated electron, where q is the elementary charge, g is the *Landé* g factor and m_e the mass of the electron. Therefore, the atomic magnetic moment is

$$\boldsymbol{\mu}_\mathrm{m} = \gamma\, \mathbf{J}, \tag{3}$$

where $\mathbf{J}$ is the total atomic angular momentum. The magnetisation $\mathbf{M}$ of solid materials is described by the sum of all magnetic moments per volume V

$$\mathbf{M} = \frac{\sum_i \mathbf{m}_i}{V} \tag{4}$$

and relates to an applied magnetic field $\mathbf{H}$ in linear materials by

$$\chi = \mathbf{M}/\mathbf{H}, \tag{5}$$

where χ is referred to as the susceptibility, which defines the magnetic response of a material to an externally applied magnetic field $\mathbf{H}$ [18, 19].

1.1.1 Magnetic behaviour of materials

The theory in this section is based on [18–20].

Diamagnetism

Materials that exhibit minimal and opposing responses to an applied magnetic field are classified as diamagnetic materials, with a very low and negative susceptibility. The magnetisation points in the opposite direction of the applied magnetic field and has a low magnitude, $|\chi| \ll 1$. Common diamagnetic atoms and materials are noble gases or ionic solids. Ideal superconductors are a unique type of diamagnets with a susceptibility of $\chi = -1$.

Paramagnetism

Materials with non-zero magnetic moments, in which the orientations are randomly distributed at room temperature and do not interact with neighbouring magnetic moments, show a net magnetisation $\mathbf{M} = 0$. Because the thermal energy is high enough to randomise the orientation of the magnetic moments. In an applied magnetic field the magnetic moments orient themselves along the direction of the field, to minimise the *Zeeman* energy, but no spontaneous magnetisation occurs. Thus, the susceptibility $|\chi| < 1$ is positive, small and inversely proportional to the temperature.

Ferromagnetism

As well as paramagnetic materials, ferromagnets contain atoms with a net magnetic moment. Unlike in paramagnets, the magnetic moments in ferromagnetic materials interact with each other via the exchange interaction which can be described as

$$E_{ij}^{\mathrm{ex}} = -J\mathbf{S}_i \cdot \mathbf{S}_j, \tag{6}$$

with the exchange integral J and the spins of interacting atoms $\mathbf{S}_{i,j}$. It has a quantum mechanical origin and leads to a parallel orientation of neighbouring magnetic moments in localised regions called domains. Below a critical temperature, which is called the *Curie* temperature, T_{c}, and in the absence of an external field, the magnetisation of the domains is non-zero $|\mathbf{M}| > 0$ and oriented in a way, that the effective magnetisation of the macroscopic material is minimised, due to the demagnetising field (discussed in more detail below) leading to a spontaneous magnetisation. When an external magnetic field is applied, more and more domains begin to align along the magnetic field with increasing field strength up to a point where all magnetic domains point along the applied field direction, which is called saturation magnetisation, M_{s}. When the field is changed in the reverse direction the response of the magnetisation would not follow the same curve. This behaviour is called hysteresis and dependent on many material parameters, as well as the magnetisation history. Ferromagnetic materials with a temperature $T > T_c$, show paramagnetic behaviour, because the thermal energy, which randomly orients the direction of the magnetic moments, overcomes the exchange energy.

Ferrimagnetism

Ferrimagnets are materials that possess two or more ferromagnetic sub-lattices. The negative exchange integral between different atomic species within the lattice results in an anti-parallel arrangement of the different species. The magnetic moment of the atoms in the sub-lattices is dissimilar. Therefore, the effective magnetisation in the domains result in $\mathbf{M} > 0$, if $T < T_c$. Macroscopically, ferrimagnets exhibit similar behaviour to ferromagnets, but with a lower net magnetisation than the sub-lattices would have individually. The most commonly used ferrimagnetic material for the investigation of spin waves is yttrium iron garnet, which is also utilised in this study.

Antiferromagnetism

This behaviour is observed in materials, with two ferromagnetic sub-lattices where the magnetic moments are equal in magnitude for each species, exhibiting negative interaction due to a negative exchange integral. Consequently, the magnetic moments favour anti-parallel alignment and are distributed such that $\mathbf{M} = 0$.

1.1.2 Demagnetising field

As previously discussed, the orientation of magnetic domains in ferromagnetic bodies with many domains results in an effective magnetisation of the entire sample being minimised due to total energy minimisation. This effect creates a magnetic field, called the demagnetising field $\mathbf{H}_{\text{dem}}$. For bodies of isotropic shape the assumption of $\mathbf{M} = 0$ applies. Ferromagnets of anisotropic shape create a magnetic field which is non-zero, and dependent on the shape of the sample, called shape anisotropy [21]. For simple geometries it can be described as

$$\mathbf{H}_{\text{dem}} = \hat{\mathbf{N}} \cdot \mathbf{M}, \tag{7}$$

with $\hat{\mathbf{N}}$ the demagnetisation tensor. For an infinite plane in the x-y direction or an infinite rod in the z-direction the demagnetisation tensor would be

$$\hat{\mathbf{N}}_{x-y-\text{plane}} = \begin{pmatrix} 0 & 0 & 0 \\ 0 & 0 & 0 \\ 0 & 0 & 1 \end{pmatrix}, \quad \hat{\mathbf{N}}_{z-\text{rod}} = \begin{pmatrix} 1/2 & 0 & 0 \\ 0 & 1/2 & 0 \\ 0 & 0 & 0 \end{pmatrix}, \tag{8}$$

which provides information about the most favourable spontaneous magnetisation direction, often referred as the easy axis, in absence of an external field and magnetocrystalline anisotropy [21–23].

1.1.3 Magnetocrystalline anisotropy

Another effect that leads to energetically more or less favourable magnetisation directions in the absence of an external field is magnetocrystalline anisotropy, which originates from spin-orbit coupling and is dependent on the crystal lattice structure of the magnetic material. For cubic lattices the anisotropy energy density can be expressed as

$$E_{\text{ani}} = K_1(m_x^2 m_y^2 + m_y^2 m_z^2 + m_z^2 m_x^2) + K_2 m_x^2 m_y^2 m_z^2 \tag{9}$$

with $K_{1,2}$ taken from experiments and $m_{x,y,z}$ are the components of the unit vector $\mathbf{m}$ parallel to the magnetisation

$$\mathbf{m} = \frac{\mathbf{M}}{|\mathbf{M}|}. \tag{10}$$

K_1 can be either positive or negative, whit the effect that the easy axes are either along the (100) or the (111) direction [21].

1.1.4 Effective field

The magnetisation of the magnetic sample aligns with the effective field, which is the sum of all fields generated by the contributing energies

$$\frac{\mathbf{M}_{\text{eff}}}{\mu} = \mathbf{H}_{\text{eff}} = \mathbf{H}_{\text{ext}} + \mathbf{H}_{\text{dem}} + \mathbf{H}_{\text{ani}} + \mathbf{H}_{\text{ex}} + ..., \tag{11}$$

where μ denotes the permeability of the material, $\mathbf{H}_{\text{ani}}$ represents the magnetic field created by the crystalline anisotropy effect, $\mathbf{H}_{\text{dem}}$ previously referred to as the demangetising field, $\mathbf{H}_{\text{ex}}$ signifies the field created by the exchange energy and $\mathbf{H}_{\text{ext}}$ refers to the applied external field. There are more contributing energies which are not taken into account [24].

1.2 Magnetisation dynamics

When subjected to a time-varying external magnetic field, magnetic materials display a dynamic magnetisation response. This section will discuss these dynamics.

1.2.1 Larmor precession

Similar to a tilted gyroscope that precesses around a gravitational force, a magnetic moment **m** that is tilted with respect to a homogeneous magnetic field **H** will precess around that magnetic field. The torque acting on the magnetic moment can be described as

$$\boldsymbol{\tau} = \mathbf{m} \times \mathbf{H}. \tag{12}$$

As the torque is equal to the time derivative of the angular momentum, the equation of motion for the atomic magnetic moment in a magnetic field can be written as

$$\frac{d\mathbf{J}}{dt} = \frac{1}{\gamma}\frac{d\boldsymbol{\mu}_\mathrm{m}}{dt} = \boldsymbol{\mu}_\mathrm{m} \times \mathbf{H}, \tag{13}$$

with γ the gyromagnetic ratio and $\boldsymbol{\mu}_m = \gamma\mathbf{J}$. Replacing the atomic magnetic moment with the magnetisation field, leads to the *Landau-Lifschitz* equation:

$$\frac{d\mathbf{M}}{dt} = \gamma\mathbf{M} \times \mathbf{H}_\mathrm{eff}, \tag{14}$$

with the previously defined effective field $\mathbf{H}_\mathrm{eff}$ [19]. The precessional motion of a tilted magnetic moment in an homogeneous magnetic field is represented schematically in Figure 1a.

1.2.2 Landau-Lifshitz-Gilbert equation

According to the *Landau-Lifshitz* equation, once the magnetic moments brought out of their equilibrium position, they would precess forever and never align along the effective field again. Because of various physical phenomena this is not the case, therefore a viscous damping term is introduced, which relaxes the magnetic moment in a spiral motion back to it's equilibrium:

$$\frac{d\mathbf{M}}{dt} = \gamma\mathbf{M} \times \mathbf{H}_\mathrm{eff} + \frac{\alpha}{M_\mathrm{s}}\left(\mathbf{M} \times \frac{d\mathbf{M}}{dt}\right). \tag{15}$$

This extension of Equation 14 is called the *Landau-Lifshitz-Gilbert (LLG)* equation. To satisfy energy conservation, the energyloss which is described via the viscous damping term partly transfers to the crystal lattice as thermal vibrational motion via phonon-magnon scattering and spin-orbit coupling [19, 25]. Further, the energy can be dissipated in magnon-magnon scattering, where one magnon, which is the single quanta of a spin wave (SW), scatters into two magnons with half the energy. A shematic representaion of the spiral motion predicted by the LLG equation is shown in Figure 1b.

1.3 Spin waves

The energy of the precessional motion can be transferred to neighbouring magnetic moments via the dipolar or exchange interactions. This leads to a collective excitation of phase shifted precessing magnetic moments, which is called a spin wave, with its quanta magnons. The wavelength λ of the spin wave is the minimal distance between two magnetic moments which are precessing

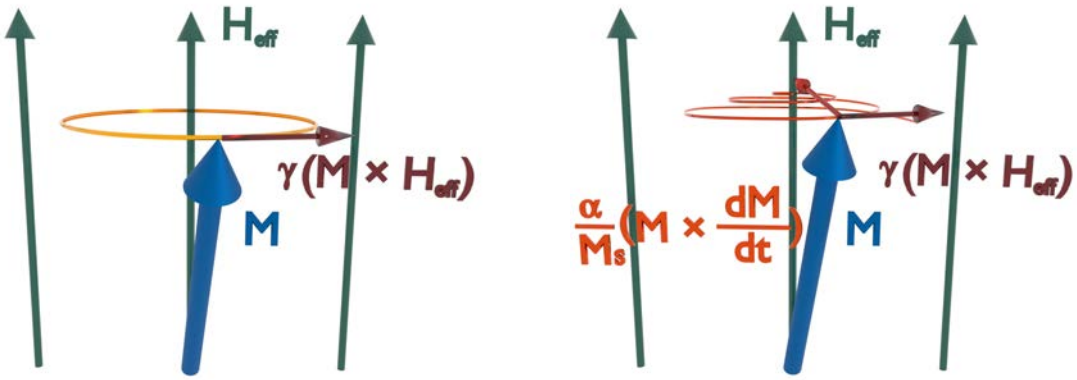

Figure 1: (a) Schematic representation of the *Landau-Lifshitz* equation, (b) schematic representation of the LLG equation.

in phase, which is illustrated in Figure 2 [19]. In the long wavelength regime (small wavevector **k**), the origin of spin waves is dominated by dipole-dipole interaction and can be described using Maxwell's equations. These spin waves are often referred to as magnetostatic spin waves (MSWs). It is important to note that the term 'magnetostatic' refers to the use of magnetostatic approximations of Maxwell's equations to describe MSW. This is because the electromagnetic (EM) wave has a much longer wavelength than a spin wave of the same frequency [4]. In the limit of $\lambda \to \infty$ (the wavevector $\mathbf{k} \to 0$) all magnetic moments precess in phase. This phenomenon is known as ferromagnetic resonance (FMR). To excite spin waves, an electromagnetic wave can be used. A simple experimental approach is to place a microstrip transmission line near a ferromagnetic material and apply an oscillating current. The transfer of power from the electromagnetic signal to the spin-wave signal is maximised during FMR [19, 24].

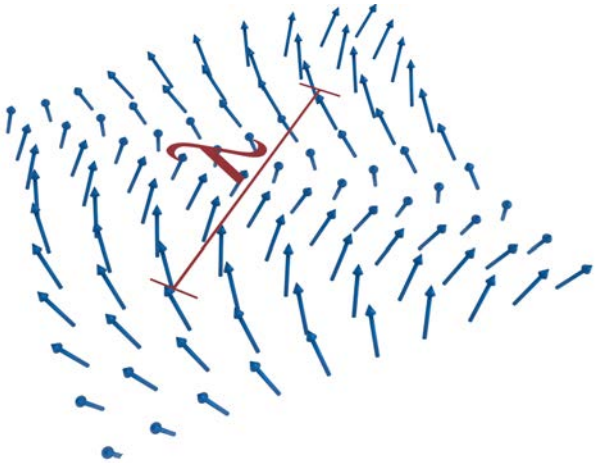

Figure 2: Illustration of a collective excitation of precessional motion of magnetic moments (spin wave) and the SW wavelength λ.

1.4 Spin waves in thin films

In ferromagnetic thin films, with hundreds of nanometer thickness, there are three distinct classes of MSW which can be excited. They vary in the orientation of the applied magnetic field relative to the direction of propagation and show different dispersion relations [4]. The first theoretical description of these wave was provided by *Damon* and *Eshbach* [26].

Forward volume magnetostatic spin waves (FVMSW)

When a static magnetic field is applied to a thin film in the out-of-plane direction, like it is shown in Figure 3a on the left (e.g. the thin film in the x-y-plane and the field pointing in the z-direction), the spin waves propagate isotropically along the film, disregarding the crystalline anisotropy, i.e. $k_x = k_y$. An analytical approximation of the dispersion relation, while not taking into account the exchange interaction, can be derived [4]:

$$f_{\mathrm{FVMSW}}(k) = \sqrt{f_{\mathrm{H}}\left(f_{\mathrm{H}} + f_{\mathrm{M}}\left(1 - \frac{1-\exp(-kd_0)}{kd_0}\right)\right)}. \tag{16}$$

Here d_0 is the thickness of the thin film, $f_{\mathrm{M}} = \gamma M_0$ and $f_{\mathrm{H}} = \gamma H_{\mathrm{eff}}$ with M_0 the saturation magnetisation, H_{eff} the effective magnetic field, k the wavenumber and γ the electron gyromagnetic ratio.

Backward volume magnetostaic spin waves (BVMSW)

The propagation direction of the SW is non-isotropic in a thin film when the magnetic field is applied in plane (for instance the field is applied in x or y direction with the film in the x-y-plane), which is illustrated in Figure 3a. When $\mathbf{k} \parallel \mathbf{H}_{\mathrm{eff}}$ the SWs are referred to as BVMSW, and are described with the analytical approximation

$$f_{\mathrm{BVMSW}}(k) = \sqrt{f_{\mathrm{H}}\left(f_{\mathrm{H}} + f_{\mathrm{M}}\frac{1-\exp(-kd_0)}{kd_0}\right)}. \tag{17}$$

Where d_0, f_{M} and f_{H} are defined equally as in Equation 16 [4].

Magnetistaic surface spin waves (MSSW)

Unlike FVMSW and BVMSW, which are volume modes and exhibit a cosinusoidal distribution of the precessional motion over the thickness, MSSW are localised to either the top or the bottom surface and decrease exponentially through the thickness of the film. For MSSW, which are often referred to as the *Damon-Eshbach* mode, the magnetic field $\mathbf{H}_{\mathrm{eff}}$ direction must be in-plane and $\mathbf{k} \perp \mathbf{H}_{\mathrm{eff}}$. The dispersion relation is approximated as

$$f_{\mathrm{MSSW}}(k) = \sqrt{\left(f_{\mathrm{H}} + \frac{f_{\mathrm{M}}}{2}\right)^2 - \left(\frac{f_{\mathrm{M}}}{2}\right)^2 \exp(-2kd_0)}, \tag{18}$$

with the same definition of d_0, f_M and f_H as above [4]. In Figure 3a the different geometries of MSW are illustrated, with the corresponding analytical approximation of the dispersion relation plotted in Figure 3b.

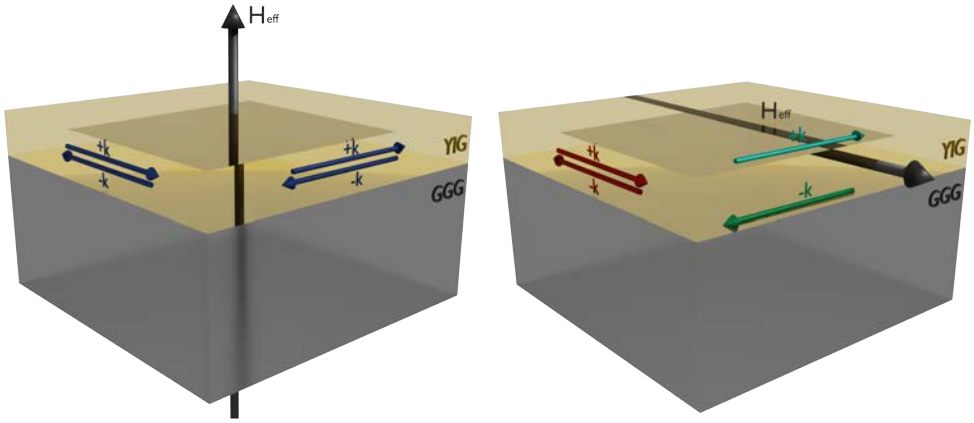

(a)

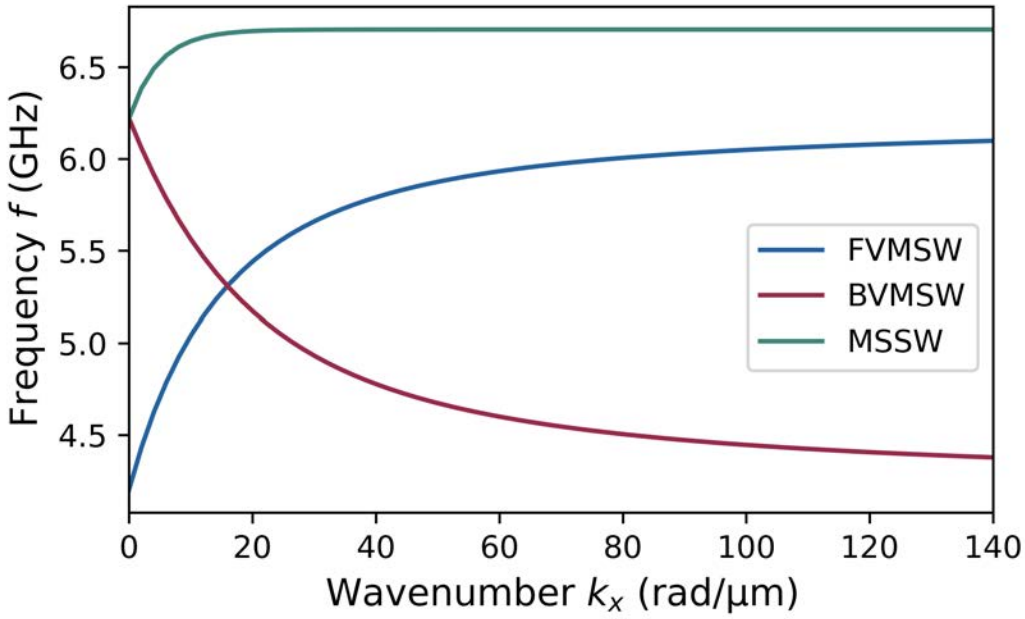

(b)

Figure 3: (a) Illustration of magnetostatic spin-wave modes in an yttrium iron garnet structure on a gadolinium gallium garnet substrate. Left picture represents FVMSW with a magnetic field pointing out-of-plane and the isotropical SW propagation direction along the film represented by the blue arrows $\mathbf{k}+$ and $\mathbf{k}-$. Right picture represents BVMSW with a SW propagation direction parallel (red arrows $\mathbf{k}+$ and $\mathbf{k}-$) and MSSW with a SW propagation direction perependicular (green arrows $\mathbf{k}+$ and $\mathbf{k}-$) to the in-plane magnetic field. (b) Analytical approximation of the dispersion relation of FVMSW, BVMSW and MSSW modes at an external field strength of 200 mT in a 50 nm thick yttrium iron garnet film [4].

1.5 Yttrium iron garnet

The material of choice to mediate SWs is yttrium iron garnet ($Y_3Fe_5O_{12}$, YIG), because it has the lowest magnetic damping for any known magnetic material. In this thesis I use 48 nm thick YIG which is grown on a gadolinium gallium garnet ($Gd_3Ga_5O_{12}$, GGG) substrate by liquid-phase epitaxy (LPE). In Figure 4a a picture of 48 nm-thick YIG grown on 500 µm-thick GGG and cut into 8×7 mm samples is shown. Furthermore, YIG is an insulator and has ferrimagnetic properties with a saturation magnetisation of $M_s = 144 \times 10^3$ A/m $= 181$ mT and damping parameters α from 2×10^{-4} to 8×10^{-4} at room temperature [27]. Because of its insulating properties, YIG has not free electrons, therefore no energy can dissipate from the SWs into to electronic system, which results in such low magnetic damping values. The crystallographic structure of YIG, as shown in Figure 4b, is complicated with a unit cell consisting of 160 atoms and a lattice constant of $a_L = 12.376$ Å [28]. The well matching lattice constant of GGG of $a_L = 12.383$ Å is the reason why it is used as a substrate to grow YIG on [29].

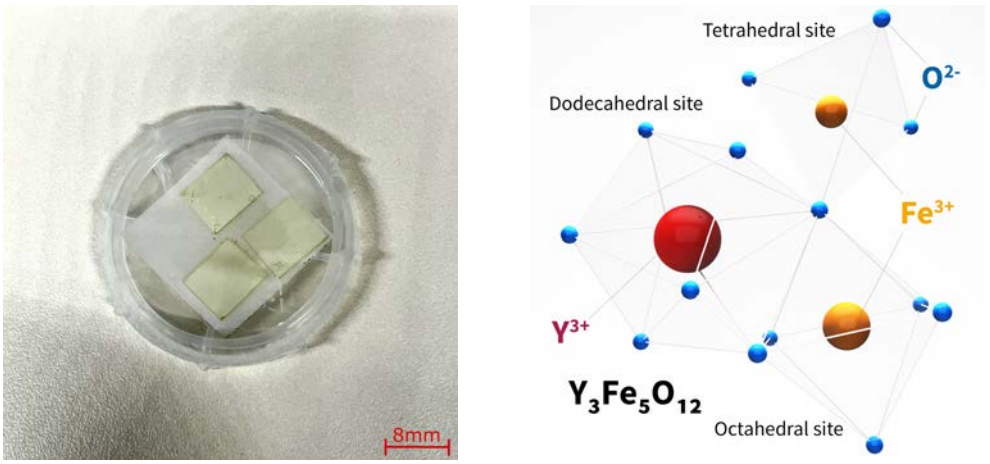

(a) (b)

Figure 4: (a) 8×7 mm samples of 48 nm-thick YIG grown on 500 µm-thick GGG. (b) Atomic structure of YIG.

1.6 Microwave engineering

In this thesis I used EM waves in the frequency range of 1 to 20 GHz to induce oscillating magnetic fields which excite propagating spin waves (PSWs) in thin films. The basics of microwaves and general design methods in radio frequency (RF) engineering are discussed in this section.

1.6.1 Skin effect

When an alternating current (AC) is applied in transmission lines with high conductivity a physical phenomenon called the skin effect needs to be considered. It reduces the effective conducting area of a wire to its outer regions of a certain thickness. To understand the skin effect we start with Maxwell's first and second equation:

$$\nabla \times \mathbf{H} = \mathbf{J} + \frac{\partial \mathbf{D}}{\partial t} \tag{19}$$

$$\nabla \times \mathbf{E} = -\mu_0 \frac{\partial \mathbf{H}}{\partial t} \tag{20}$$

with **H** the magnetic field, **J** the current density, **D** the electric displacement field, **E** the electric field and μ_0 the vacuum permeability. According to these equations, a current flowing trough a conducting wire induces a circular magnetic field outside and inside the wire. When an AC current is applied, the magnetic field, like the electric field, is time-oscillating. The time-harmonic magnetic field induces eddy currents in the wire, which counteracts the applied current in the centre of the wire and reinforces it on the surface of the wire, as it is shown in Figure 5.

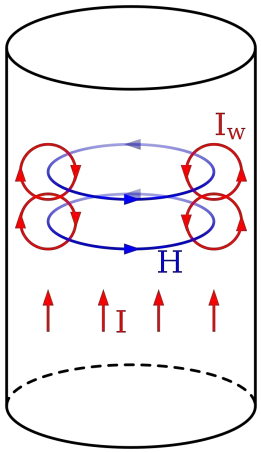

Figure 5: Illustration of the cause of skin effect. The oscillating current I is inducing the magnetic field H, which, when it is changing, induces eddy currents I_w which oppose I in the middle and reinforces it at the skin of the wire (taken from [30]).

The distribution of the electric field density along the radius of the wire cross section is given by

$$E(z) = E_0 \cdot \exp(-(1+i)z/\delta), \tag{21}$$

where z is the direction along the radius of the wire cross section and δ is the skin depth, at which distance the electric field density is reduced to $1/e$ of it's surface value and is defined as

$$\delta = \sqrt{\frac{2}{\omega\sigma\mu_0}}, \tag{22}$$

with ω the current's angular frequency and σ the conductivity of the current carrying material. Due to the skin effect, the effective area in a cylindrical conductor reduces in a frequency-dependent manner across the cross-section. The reduction of the effective area reduces the total conductivity of the conductor, which is directly related to the area [31].

1.6.2 Characteristic impedance

Let us consider two conducting wires, which are placed next to each other and equal currents $I^+(t)$ and $I^-(t)$ flow in opposite directions. An electric field is generated between the conductors, which, together with the perpendicular magnetic field induced by the current, creates a transient electromagnetic wave that travels along and between the two wires, if $I^{\pm}(t)$ is a transient signal [31]. The setup can be viewed as an electric circuit, as illustrated in Figure 6. The inductance L represents the magnetic field, while the capacitance C represents the electric field. The resistance R and conductance G represent the ohmic resistance of the wires and the losses

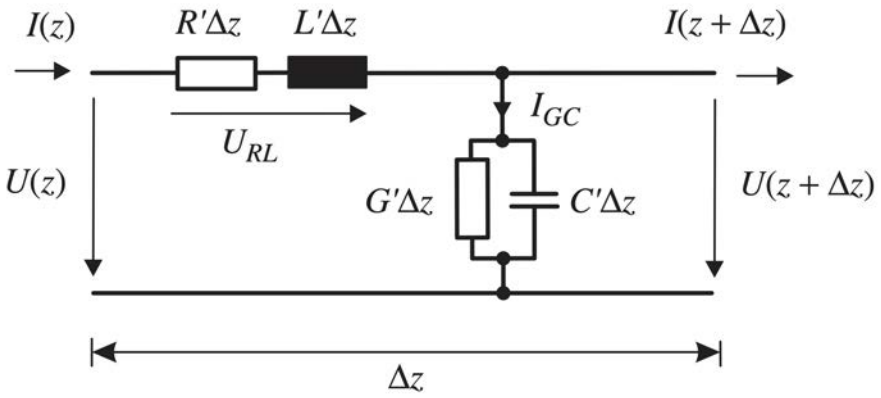

Figure 6: Equivalent circuit of two conducting wires placed next to each other (taken from [31]).

of energy through the space between the two conductors, respectively. These variables can be defined as quantities per unit length Δz, with the relations given as follows:

$$L' = \frac{L}{\Delta z},\ C' = \frac{C}{\Delta z},\ R' = \frac{R}{\Delta z},\ G' = \frac{G}{\Delta z}. \tag{23}$$

The characteristic impedance Z_0 of such a system can then be defined as

$$Z_0 = \sqrt{\frac{R' + i\omega L'}{G' + i\omega C'}}, \tag{24}$$

with ω the current's angular frequency. Detailed derivation of Equation 24 can be found in [31].

To transmit RF signals with low losses from the source to devices, it is important to match the characteristic impedance (i.e. $Z_{\text{input}} = Z_{\text{load}}$). In the ideal case of a perfect signal transmission the electromagnetic wave is transmitted and not reflected on device intersections, where the reflection coefficient at the load device can be defined as

$$r_{\text{load}} = \frac{Z_{\text{load}} - Z_{\text{input}}}{Z_{\text{load}} + Z_{\text{input}}}. \tag{25}$$

In laboratories an impedance of $Z = 50\,\Omega$ is common, because of a compromise between the maximum transmitted power possible at an impedance of $Z = 30\,\Omega$ and the lowest losses at and impedance of $Z = 77\,\Omega$ [31].

1.6.3 Transmission lines

To achieve the characteristic impedance of choice the correct materials in combination with the right design need to be chosen. There are many simple ways to achieve a transmission line with a design related adjustable impedance. Two of the methods that will be used in this thesis are discussed below.

Coaxial line

The cable of choice when it comes to laboratory setups in the field of RF engineering are coaxial cables. Because of their design they are shielded against outside radiation, as well as bendable down to a certain radius. Coaxial lines consist of a cylindrical shaped signal line, surrounded by

a dielectric material and a conducting shell on the outside, acting as the ground line. A cross-sectional illustration of a coaxial cable can be found in Figure 7. The characteristic impedance of these cables can be tuned by the choice of the dielectric material separating the signal and ground line, and the dimensions of the signal line and the radial distance between signal and ground line.

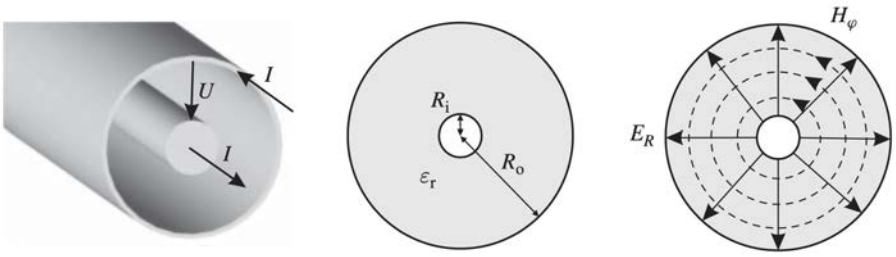

Figure 7: Cross-sectional view of a coaxial cable with the associated electric (solid line) and magnetic (dashed line) field lines (taken from [31]).

Coplanar line

When a transmission line is required on substrate, coplanar lines, also known as coplanar waveguides (CPWs), are often used. CPWs consist of a signal strip and two ground strips located on the same plane, as shown in Figure 8. In some variations of this design, the ground line can extend to the bottom of the substrate, but this is mostly limited to the fabrication method. The electromagnetic wave is travelling between the signal and ground lines [31]. When working with on-chip integrated signal lines in small sizes, the design of choice are CPWs as they can be deposited on different substrates, with lithography methods and the dimensions of the design allows to achieve impedance matching easily.

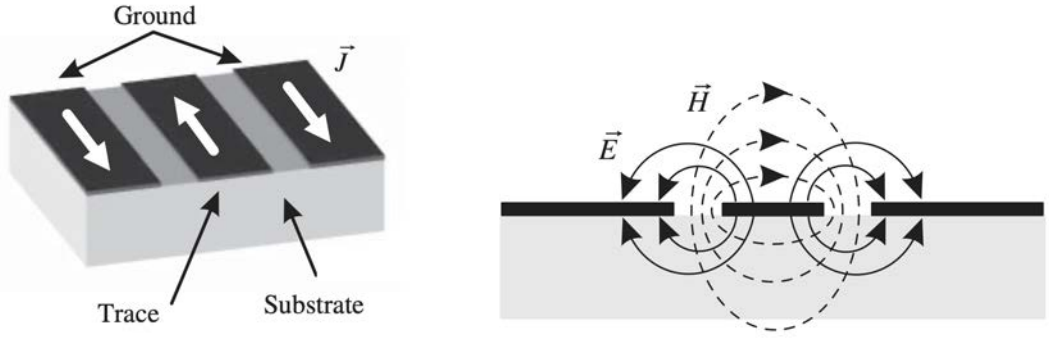

(a) (b)

Figure 8: (a) Coplanar waveguide segment on a substrate with (b) the associated electric (solid line) and magnetic (dashed line) field lines. Trace line represents the signal line (both taken from [31]).

1.6.4 S-Parameters

RF devices can be characterised by a multi-port network, which is described by the scattering matrix of transmission. In this work the description for the network with a two-port system is

sufficient. In that case the S-matrix is defined as,

$$\begin{pmatrix} b_1 \\ b_2 \end{pmatrix} = \begin{pmatrix} S_{11} & S_{12} \\ S_{21} & S_{22} \end{pmatrix} \begin{pmatrix} a_1 \\ a_2 \end{pmatrix} \tag{26}$$

with a_1 and a_2 the input signal power of port 1 and port 2 and b_1 and b_2 the output signal power of port 1 and port 2 respectively. The parameters of the matrix are specified as, S_{11} the reflection coefficient at port 1, S_{22} the reflection coefficient at port 2, S_{21} the transmission coefficient from port 1 to port 2 and S_{12} the reverse transmission coefficient from port 2 to port 1. In the case of reciprocal devices, $S_{21} = S_{12}$ holds [32].

1.7 Antennas for spin-wave excitation and detection

The simplest way to excite and detect PSWs experimentally is to place a transmission line on the surface of a ferromagnetic thin film and apply a frequency dependent electrical signal in the transmission line [19]. The lateral sizes of the signal line should match the spin-wave wavelength which are supposed to be excited. In Figure 9 *Fourier* transforms of the current distribution in a stripline and a CPW antenna, which are illustrated on the left side of the image, is plotted. This transformation of the current distribution is an approximation of the actual SW excitation efficiency dependent on the antennas design [17]. In Figure 9b the signal and ground lines had a width of 200 nm and are 1 µm apart. Further, the theoretical SW transmission T can be calculated by

$$T = \tilde{J}_{exc}^2 \cdot \exp(-x/\lambda_D), \tag{27}$$

with $\tilde{J}_{exc}$ the *Fourier* transformation of the current distribution of the excitation antenna, x the propagation length and λ_D the decay length. The decay length is proportional to $l_{decay} \propto v_{gr}/\alpha f$, with v_{gr} the SW group velocity, α the *Gilbert* damping and f the SW frequency [5]. Additionally, it is important to notice that the current in the transmission line is not the cause for the SW excitation but rather the magnetic field induced by the current distribution is. Apparently this magnetic field is of a different shape than the current distribution. A more accurate investigation of the SW excitation spectrum is conducted in Section 2 and Section 4.

Figure 10 shows an illustration of a stripline antenna placed on a YIG film, with applied AC current $\mathbf{I}_{\text{in}}(\omega)$. The AC current in the stripline induces an oscillating magnetic field $\mathbf{H}_{\text{ex}}(\omega)$ circulating around the transmission line. This magnetic field changes the effective field $\mathbf{H}_{\text{eff}}$ which will drive the magnetic moments to precess and thus excite a SW. The SW will propagate in both directions away from the transmission line. At a certain distance, a second transmission line is placed on the YIG film, which sees a oscillating magnetic field $\mathbf{H}_{\text{out}}$ once the PSW reaches the antenna. This will induce an oscillating current $\mathbf{I}_{\text{out}}(\omega)$, which can be detected as an RF signal. This method to excite and detect spin waves is often referred to as all electrical propagating spin-wave spectroscopy (AEPSWS).

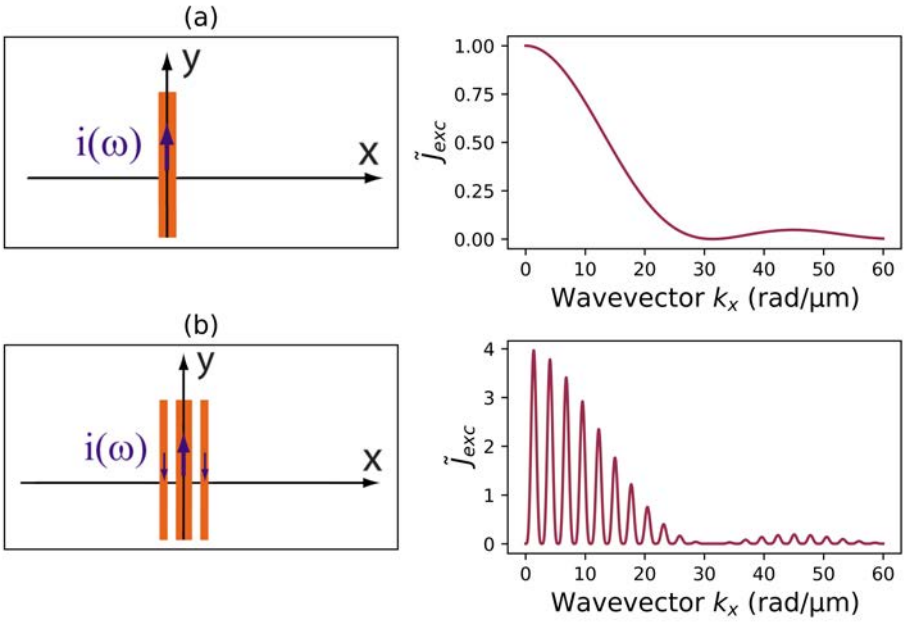

Figure 9: Fourier transform of the current distribution of (a) a stripline antenna and (b) a CPW antenna [17].

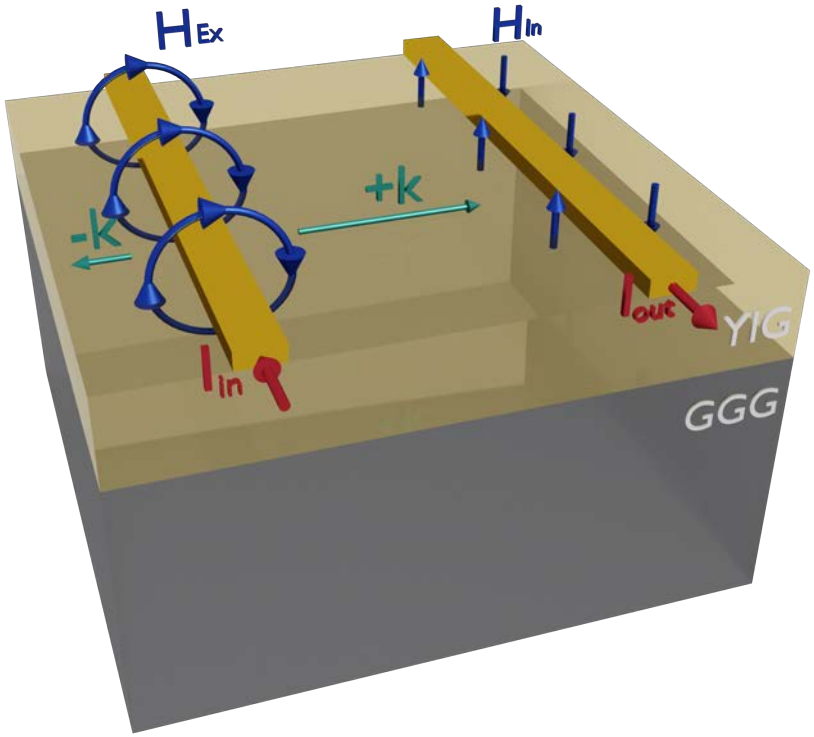

Figure 10: Current $\mathbf{I}_{in}(\omega)$ applied in stripline antenna placed on YIG film induces magnetic field $\mathbf{H}_{ex}(\omega)$, which excites PSWs with k-vectors k_+ and k_-. The PSW induces a magnetic field $\mathbf{H}_{out}(\omega)$ at a neighbouring stripline antenna which generates the output current $\mathbf{I}_{out}(\omega)$.

2 Computational methods

Numerical calculations are essential for designing on-chip antennas for all-electrical propagating spin-wave spectroscopy. The goal is to obtain an efficient antenna design that increases the coupling rate between the microwave and the SW signal. In this section I explain and discuss the numerical methods used in this thesis, including the finite element method (FEM) and finite difference method (FDM). These methods are used to conduct electromagnetic and micromagnetic simulations. At the end of this section I present and analyse the gained results.

2.1 Finite element and finite difference methods

To solve differential equations numerically, the two main methods to discretise the problem are the finite element- and the finite difference method. In the FEM the 3-dimensional structure, for which the equations need to be solved, does not underlie any geometry constraints. The discretisation is based on dividing the geometry in tetragonal cells, which allows a more accurate mimic of complex structures than compared to the FDM. However, the higher demand for memory and the slower computation speed is a major disadvantage of FEM compared to FDM.

FDM divides the geometry into an orthogonal array of cubic cells. It is commonly used in simple, cubic-like structures or calculations requiring high computation speed. However, on geometries with non-orthogonal edges, FDM can result in higher inaccuracies than the FEM. Two discretised spheres are represented to make the difference between FEM and FDM clear. In Figure 11a, the sphere is discretised according to the FEM, and in Figure 11b according to FDM.

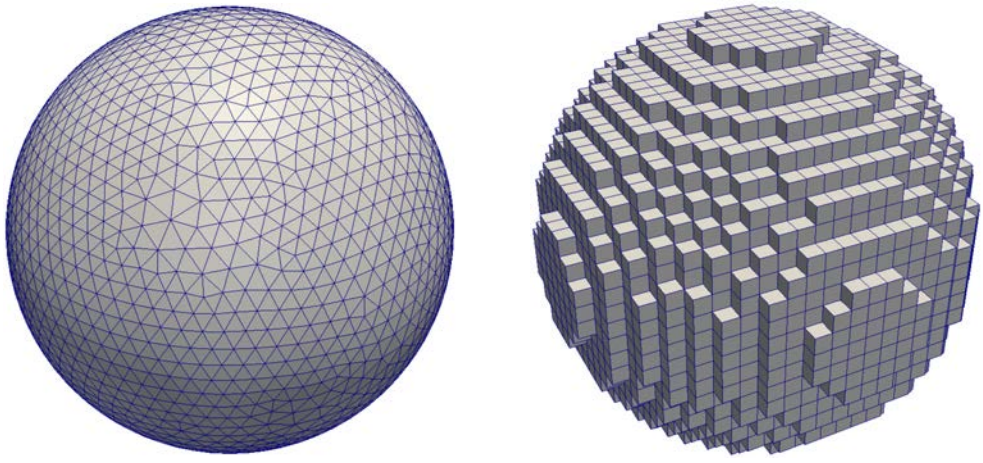

(a) (b)

Figure 11: Sphere discretised with (a) FEM and (b) FDM (taken from [33]).

2.2 Electromagnetic simulation

First, I investigated the different antenna designs in an electromagnetic simulation only, with the software package *COMSOL Multiphysics* and the built-in RF module. Then, I simulated the SW excitation efficiency with respect to different antenna designs with the python module *Magnum.np*, which will be covered in Section 2.3.

Maxwell's equation

To solve an electromagnetic problem the basis set of equations are Maxwell's equations. Maxwell's first and second equation are defined in Equation 19 and 20. The third and fourth equation are defined as

$$\nabla \cdot \mathbf{D} = \rho \tag{28}$$

$$\nabla \cdot \mathbf{H} = 0, \tag{29}$$

with $\mathbf{H}$ the magnetic field, $\mathbf{D}$ the charge distribution and ρ the charge density. In the curl-curl formulation the wave equation for the electric field $\mathbf{E}$ can be derived from Maxwell's equation

$$-\nabla \times \left(\frac{1}{\mu_0} \nabla \times \mathbf{E} + \frac{\partial \mathbf{M}}{\partial t} \right) = \sigma \frac{\partial \mathbf{E}}{\partial t} + \varepsilon_0 \frac{\partial^2 \mathbf{E}}{\partial t^2} + \frac{\partial^2 \mathbf{P}}{\partial t^2}, \tag{30}$$

where $\mathbf{P}$ is the electric polarisation vector, $\mathbf{E}$ the electric field, $\mathbf{M}$ the magnetisation, ε_0 the vacuum permittivity, μ_0 the vacuum permeability and σ the electric conductivity of the material the equation is solved for. The alternating voltage in the chosen frequency is applied to the system via the lumped port boundary condition of *COMSOL Multiphysics* (see [34] page 43). They only can be applied in a quasi-static-approximation, which includes placing the ports between two conducting objects separated by a distance much smaller than the wavelength of the electromagnetic wave. Lumped ports are easy to apply and can be utilised to calculate the S-parameters. COMSOL Multipyhsics uses two main methods to simulate time dependent physical quantities. The time-domain study calculates the variation of the solution of the set of equations in each time step, providing accurate solutions for one frequency each but requiring significant computational effort. In contrast, the frequency-domain study solves the set of equations in an implicit time-domain manner and provides static solutions for various frequencies of the applied RF signal [34]. Both methods are used in this work. The Electromagnetic Waves, Transient (temw) interface is used for the time-domain simulation and the accurate calculation of the magnetic field distribution induced by the investigated antenna for the SW excitation. For the frequency-domain simulation the Electromagnetic Waves, Frequency Domain (emw) interface is used to calculate the amount of EM power radiated and reflected by the whole design.

Geometry and materials

The simulation box consists of a 100 µm thick layer of GGG, 48 nm thick film of YIG, the structure of the different antennas in a 100 nm thick Au-layer and a 100 µm thick layer of air above. This cubical box has overall dimensions of $0.2 \times 1 \times 2.8$ mm, which is shown in Figure 12. Two lumped

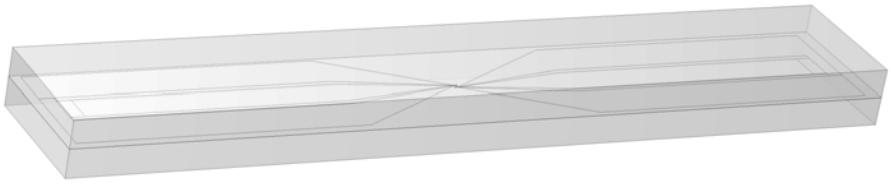

Figure 12: Geometry of the simulation box for the electromagnetic time- and frequency-domain simulation.

ports are introduced at the outer regions of the Au-structures, connecting the signal and ground

lines, of the CPW-transmission line. One lumped port acts as an excitation port, with the applied voltage function

$$\sin(2\pi \cdot 13\,\text{GHz} \cdot t) \cdot 12.8\,\text{mV}, \tag{31}$$

where t represents the time. The excitation frequency of 13 GHz is chosen to be above the highest frequency these antennas will be used for in the experimental measurements in Section 4 and the voltage amplitude of 12.8 mV is selected to equal an input power of -25 dBm for a 50 Ω matched setup. The second lumped port acts only as a receiving port, i.e. no electromagnetic wave is excited on this port. The CPW-transmission lines, on this thesis referred to as the pads, are designed to match the 50 Ω impedance of the remaining laboratory setup. The impedance of the pads along the transmission direction are calculated with the help of an analytical online calculation tool (see [35]), with the requirement to fit the distance of the used picoprobes pitch, discussed in more detail in Section 4.

Because the width of the pads are in the order of micrometres and the width of the antennas are nanometres, there is a need to reduce the structure size. This region of the geometry is named taper. To simplify the fabrication, linear tapers of 400 µm length are used. Although the impedance match of 50 Ω is not ensured along the tapers, the beginning and end are designed to match a CPW transmission line with 50 Ω or 100 Ω impedance. I simulated four different designs of antennas and tapers.

For two designs, the linear tapers are connected to a CPW transmission line of 15 µm length and 200 nm lateral size of the signal and ground lines. At the end of the CPW transmission line, the signal line is connected to the ground lines, which is referred to as the CPW antenna. One CPW antenna is matched to 50 Ω and the other one to 100 Ω impedance. The 50 Ω CPW antenna has a spacing between signal and ground line of 0.85 µm, whereas this spacing is 2.1 µm wide for the 100 Ω CPW antenna. The structure of the 100 Ω CPW antenna with the linear tapers and a fraction of the pads is figured in Figure 13. For the second two designs, the tapers are as well matched to a CPW transmission line 50 Ω and 100 Ω impedance, with the restriction that the spacing between the signal and ground line is of 15 µm length. At the end of the tapers the signal line is connected to the ground lines with a connection line of 200 nm width. These connection lines are referred to as the 50 Ω stripline and 100 Ω stripline antennas, for the tapers matched to the CPW with 50 Ω and 100 Ω impedance, respectively. The four different antenna designs are depicted in Figure 14.

Material parameters

The air domain is assigned the COMSOL built in material parameters for air. For the YIG and GGG domains, material parameters are set according to Table 1. The domain for the antenna structure is assigned material parameters of Au-thin film following [36].

Properties	YIG	GGG
Electrical conductivity σ (S/m)	10^{-6} [37]	10^{-14} [38]
Saturation magnetisation M_s (A/m)	140×10^3 [39]	805×10^3 (at $T = 0$ K) [40]
Relative permittivity ε	14 [37]	12 [41]
Relative permeability μ	32 [42]	1 [41]

Table 1: Material parameters of YIG and GGG used in the electromagnetic simulation.

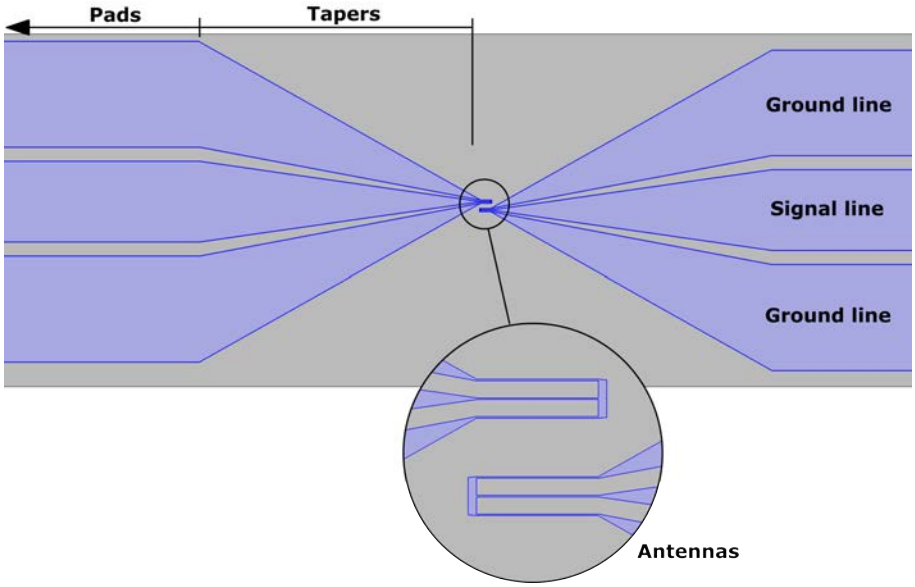

Figure 13: Specification of pads, tapers and antennas. CPW pad with the following tapers and the CPW antenna with 100 Ω impedance match.

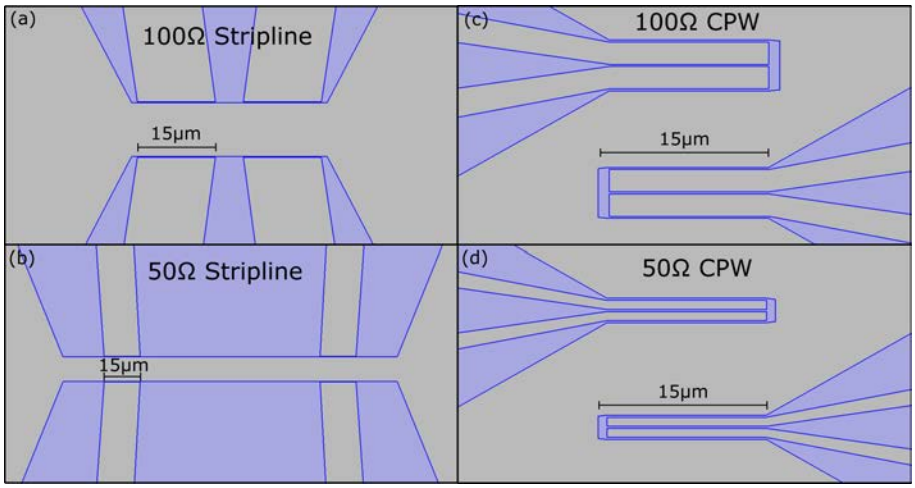

Figure 14: Design of different antennas. (a) 100 Ω stripline antenna, (b) 50 Ω stripline antenna, (c) 100 Ω CPW antenna, (d) 50 Ω CPW antenna. The length of the antennas is 15 µm, while the width of the signal and ground lines of the antennas is 200 nm respectively.

Mesh and time step

To discretise the geometry, it is necessary to create a mesh with cells small enough to obtain accurate solutions, but not too small to ensure a reasonable computational time. Firstly, the user-controlled meshing from the COMSOL software is applied. The maximum and minimum element size is set to 1 mm and 75 µm respectively, the maximum element growth rate is 1.45, the curvature factor is 0.5 and factor for the resolution of narrow regions 0.6. Second, the mesh is refined in regions where high spatial resolution is required. In this case, the antenna where the AC voltage is applied is refined, to obtain a high resolution grid of the magnetic field near the

antenna. For the frequency-domain study, the mesh is refined on of both antennas including the linear tapers and the pads. A picture of the meshed 100 Ω CPW antenna is shown in Figure 15.

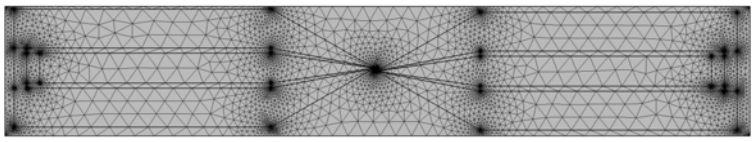

(a)

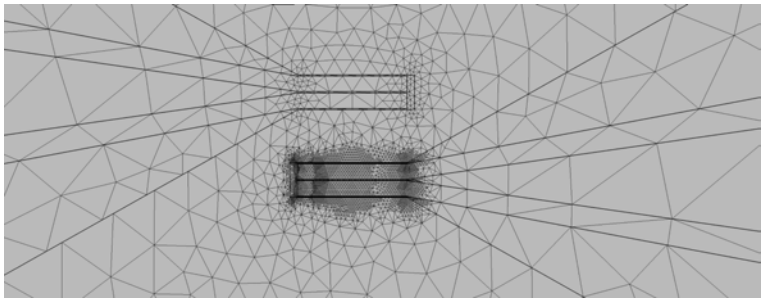

(b)

Figure 15: (a) Top view of the mesh of the whole simulation box of one example antenna and (b) the zoom-in to the small regions of the 100 Ω CPW antenna with mesh refinement.

The simulation time ranges from 0 to 0.5 ns with a time step of 0.001 ns. At this time step the *Nyquist* frequency, which gives the maximum frequency to be resolved distortion free at a certain sampling rate, is $f_N = 500\,\text{GHz}$, and the electromagnetic wave which is excited at $f_{EM} = 13\,\text{GHz}$ has 38 sampling points per period. For the frequency-domain simulation, a frequency range from 1 to 20 GHz in 200 MHz steps is chosen, to analyse the frequency range in which the antennas are used in the experimental measurements.

Transfer of FE into FD grid

To implement the magnetic field distribution created by the antenna in the micromagnetic simulation, the H-field components need to be exported. The exported data is only taken at one time step, specifically when the amplitude of the magnetic field at the antenna is at its maximum. Micromagnetic simulations also consider exchange interactions which have a short range order, therefore the cell size of the simulation box has to be smaller than the exchange length, which is about $\lambda_{ex} = 17 \times 10^{-9}\,\text{m}$ for YIG [39]. Consequently, the simulation box for the micromagnetic FDM simulation is much smaller than the electromagnetic FEM simulation to keep computation time down and the H-field is exported on an interpolated finite difference grid in the total size of the simulation box for the micromagnetic simulation. The exported FD box is illustrated in Figure 16.

2.3 Micromagnetic simulation

Of the methods used to investigate the dynamics of magnetisation in magnetic structures, the micromagnetic simulation solved with the FDM is the method of choice in this thesis, due to the mesh geometry and the computational efficiency. This technique can be used to numerically calculate the magnetisation dynamics, with the LLG equation (see Equation 15), in micro- or nanostructure with time-, space-, frequency- and phase-resolution. The used tool is the PyTorch based GPU enhanced python-package *Magnum.np* [43]. In addition, the FEM based

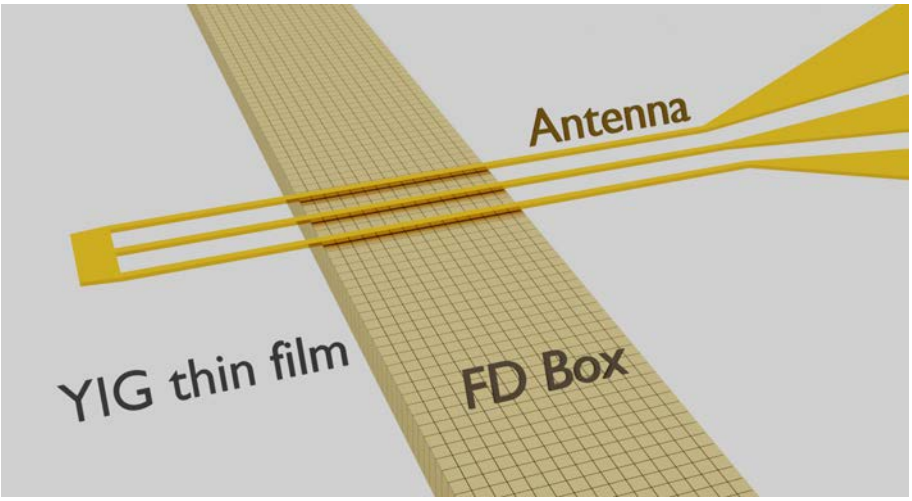

Figure 16: Exported FD box from the electromagnetic FEM simulation used in the micromagnetic FDM simulation.

micromagnetic modelling package *TetraX* is used to compare the results with its built-in SW dispersion relation calculator [44].

Fundamentals of micromagnetic simulation

Dynamic micromagnetic simulations describe the spatially resolved motion of the magnetisation in an effective field, which is realised by solving the LLG equation for every grid cell and every time step. The magnetisation field $\mathbf{m}(x, y, z)$ describes the magnetisation direction on every grid point and is constrained with the unit-sphere boundary condition $|\mathbf{m}| = 1$. The effective field is calculated by total energy minimisation of the contributing energy terms, which create the effective field. *Magnum.np* is a finite difference solver for the LLG equation, offering high customisation options for specific problems. It allows for various field contributions and provides time- and space-resolution. In the simulation the effective field includes the demagnetising field, the exchange field and the applied external field. For external field, the exported magnetic field $\mathbf{H}_{\text{dyn}}(x, y, z)$ from the electromagnetic simulation is imported and multiplied by a sinc pulse function

$$\mathrm{f}_{\text{sinc}}(t) = \frac{\sin(2\pi f_{\text{c}}(t - t_0))}{2\pi f_{\text{c}}(t - t_0)}, \tag{32}$$

to excite a wide frequency range of spin waves. In Equation 32 $t_0 = 8/f_{\text{c}}$ and f_{c} is the cutoff frequency and chosen to be at $f_{\text{c}} = 10\,\text{GHz}$, which is below the maximum MSW frequency at an static magnetic field of 150 mT. Thus, all spin waves with a frequency below 10 GHz can be excited. Furthermore, the static magnetic field adds to the external field, which results in the total external field contribution

$$\mathbf{H}_{\text{ext}}(x, y, z, t) = \mathrm{f}_{\text{sinc}}(t) \cdot \mathbf{H}_{\text{dyn}}(x, y, z) + \mathbf{H}_{\text{stat}}(x, y, z). \tag{33}$$

Geometry

As mentioned in Section 2.2, the simulation box for the micromagnetic simulation is much smaller than the one for the electromagnetic simulation. All cells are identical in size of $15 \times 15 \times 50\,\text{nm}$ in x-,y- and z- direction. The total simulation box consists of a YIG thin film with the size

of 70 µm × 1 µm × 50 nm, where the SW propagates along the x-direction. For the length in x-direction of $l = 70\,\mu m$, the fast *Fourier* transform (FFT) is applied over one line of grid points, which results in a wavevector k_x resolution of $\Delta k_x = 1/l = 0.014\,\mathrm{rad}/\mu m$. Periodic boundary condition with a repetition of 40 were applied along the width of the simulation box, resulting in an effective width of 40 µm, to mimic the SW dispersion properties of a YIG thin film, instead of a YIG waveguide.

Material

Material parameters are chosen for YIG according to [39] with a saturation magnetisation $M_s = 140 \times 10^3\,\mathrm{A/m}$ and an exchange stiffness of $A = 3.65 \times 10^{-12}\,\mathrm{J/m}$. The *Gilbert* damping parameter is set to $\alpha = 5.1 \times 10^{-4}$ [11] and raised to $\alpha = 1$ on the 20 outer cells in the lengthwise direction, to absorb the SW at the end of the simulation box and avoid reflections at the edges.

Sample initialisation

The initial conditions for the magnetisation of the sample is $\mathbf{m} = (1, 0, 0)$, and the static magnetic field is set to $\mathbf{H}_{\mathrm{stat}} = (150, 0, 0)\,\mathrm{mT}$. Although the static magnetic field $\mathbf{H}_{\mathrm{stat}}$ and the magnetisation $\mathbf{m}$ are pointing into the same direction, the magnetisation of the state is not uniform in equilibrium, due to the demagnetising field. Therefore, the built-in relax function is used to relax the sample. The sample is relaxed when the total energy of the system is minimised. Taking the relaxed state as the initial condition, the LLG equation is solved, with the applied excitation field $f_{\mathrm{sinc}}(t) \cdot \mathbf{H}_{\mathrm{dyn}}(x, y, z)$ over a period of $T = 100\,\mathrm{ns}$, which allows a frequency resolution of $\Delta f = 1/T = 10\,\mathrm{kHz}$. The solution of the magnetisation is saved every 10 ps, with a resulting nyquist frequency of $f_{\mathrm{N}} = 50\,\mathrm{GHz}$.

Data post-processing

The solution of the magnetisation dynamics are saved in every time step for every cell in an multidimensional tensor $\mathbf{m}(x, y, z, t)$. By performing an FFT for $\mathbf{m}(x, y, z, t)$, the dispersion relation of the excited SW frequency f with respect to the SW wavevector $\mathbf{k}$ can be extracted. To give a high resolution in frequency- and k-space the simulation time and the simulation box respectively must be large enough. For the dispersion relation only the z-component over one line along the SW propagation direction x of $\mathbf{m}(x, y, z, t)$ is transformed

$$\mathrm{FFT}(m_z(x, t)) = \tilde{m}_z(k_x, f). \tag{34}$$

2.4 Computational analysis

In this section, I will present and discuss the outcomes of the electromagnetic FEM and micromagnetic FDM simulation. I will analyse the results with respect to the electromagnetic leakage in the absence of any SW signal, the efficiency of SW excitation, the SW excitation spectra, and compare the dispersion relation obtained from *Magnum.np* and *TetraX*.

2.4.1 Local magnetic field of different antenna types

The geometry of the magnetic field around an antenna is crucial in determining which SW wavevectors can be excited efficiently [13, 17, 45]. Therefore, I analysed and compared the magnetic field distribution in a cross sectional view of the antennas. In Figure 17 the norm of the magnetic field $|\mathbf{H}| = \sqrt{H_x^2 + H_y^2 + H_z^2}$ on the surface of the antenna and the YIG thin film is

indicated by the colour legend and given in A/m. The time step is chosen when the magnetic field norm is at its maximum at the region around the antenna in the electromagnetic simulation. The colour bar is in the range of $0-15\,\mathrm{A/m}$ for the stripline antennas and $0-3\,\mathrm{A/m}$ for the CPW antennas. This may originate from the high impedance mismatch of the stripline antennas. As a result of the geometry change from a CPW transmission line to a connection line between the ground and signal lines of this transmission line, the impedance at this connection is unknown and most likely vary greatly compared to the $50\,\Omega$ matched CPW transmission line. This impedance mismatch leads to a high radiation of EM signal [46]. Additionally, the $100\,\Omega$ antennas induce a bigger magnetic field than the $50\,\Omega$ antennas for both types of antennas because of the impedance change from $50\,\Omega$ to $100\,\Omega$. The higher field radiation for antennas with higher impedance can also be observed in Figure 19, where the EM leakage is displayed. The EM leakage is higher for the $100\,\Omega$ antennas than for $50\,\Omega$ antennas of the same design. The Ohmic resistance is $35.9\,\Omega$ for the $100\,\Omega$ CPW antenna, $35.8\,\Omega$ for the $50\,\Omega$ CPW antenna, $15.1\,\Omega$ for the $100\,\Omega$ stripline antenna, and $12.0\,\Omega$ for the $50\,\Omega$ stripline antenna.

The magnetic field components are exported in a finite difference grid locally around the antennas as it is described in Section 2.1, averaged over the box width and plotted along the length of the exported box shown in Figure 18. The distance on the x-axis of the upper plots represents the distance from the centre of antennas signal line. The lower two plots show the FFT of the exported signal. We observe that the maximum value of the magnetic field norm is ten times higher for the stripline antennas with a maximum of value $7.45\,\mathrm{A/m}$ than for the CPW antennas with a maximum value of $0.76\,\mathrm{A/m}$. This finding is most likely caused by the higher Ohmic resistance of the CPW antennas, because an increase in Ohmic resistance decreases the current density which decreases the induced magnetic field around the antenna. The FFT of the magnetic field distribution, provides an estimate of the SW excitation efficiency with respect to the SW wavevector k_x. Although the magnitude of the magnetic field is ten times smaller for the CPW antennas than for the stripline antennas, the FFT of the magnetic field distribution is approximately five times smaller for the CPW antennas than for the stripline antennas, which is caused by the additional narrower field peaks caused by the ground lines of the CPW antennas, which is also the cause of the specific peaks which can be excited. For the $50\,\Omega$ CPW antenna these peaks are broader and further apart than for the $100\,\Omega$ antenna, caused by the smaller distance between ground and signal lines. Moreover, it can be seen that the field distribution of the $100\,\Omega$ stripline antenna is sharper and higher with $7.45\,\mathrm{A/m}$ than for the $50\,\Omega$ stripline antenna which reaches a value of $5.04\,\mathrm{A/m}$. This results in an higher SW excitation efficiency for higher wavevectors k.

2.4.2 Electromagnetic leakage and reflection

To investigate the antenna structures with respect to many different excitation frequencies I performed an electromagnetic wave, frequency domain study. The Au-structure is treated as a perfect electric conductor in this simulation to reduce the complexity of the simulation and safe computational effort, which implies the Au-structure has zero resistance. Due to the lower number of computational steps in the frequency domain study (100 frequency steps, as opposed to 400 time steps in the time domain study), I was able to refine the mesh by a factor of two while maintaining a similar level of computational effort. The electromagnetic leakage, i.e. the power of the EM signal which is emitted from the excitation antenna and taken up from the receiving antenna can be represented with the S_{21}-parameter. This parameter for the different antenna structures in a frequency range of $1-20\,\mathrm{GHz}$ is displayed in Figure 19 in dB-scale. The S_{11}-parameter represents the signal which is reflected back to the sending

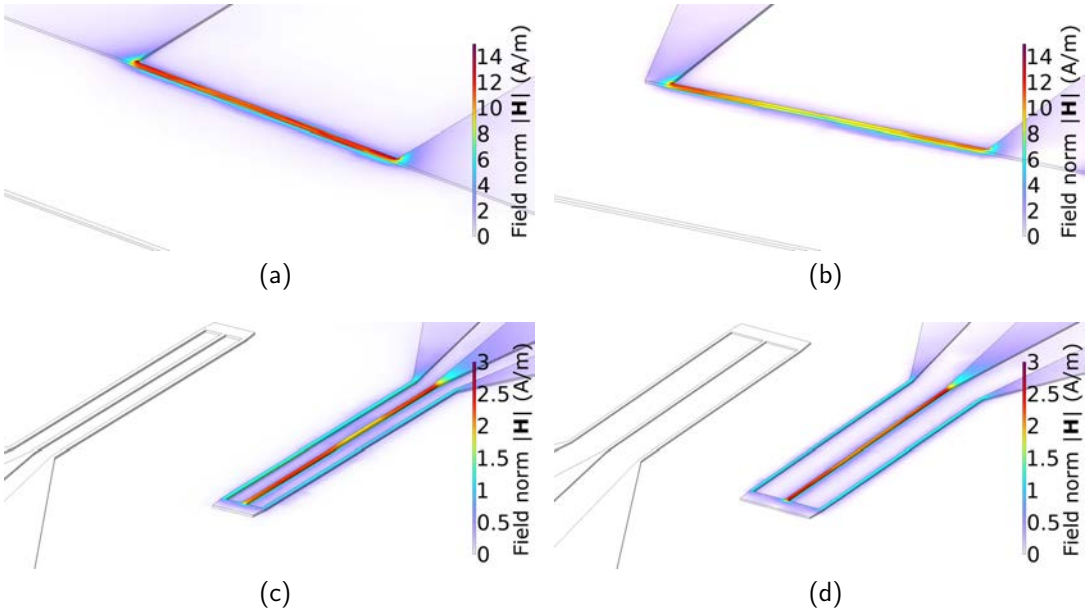

Figure 17: Norm of the magnetic field on the surface of the Au and YIG structure in A/m of different antennas simulation results. (a) 50 Ω stripline antenna, (b) 100 Ω stripline antenna, (c) 50 Ω CPW antenna and (d) 100 Ω CPW antenna.

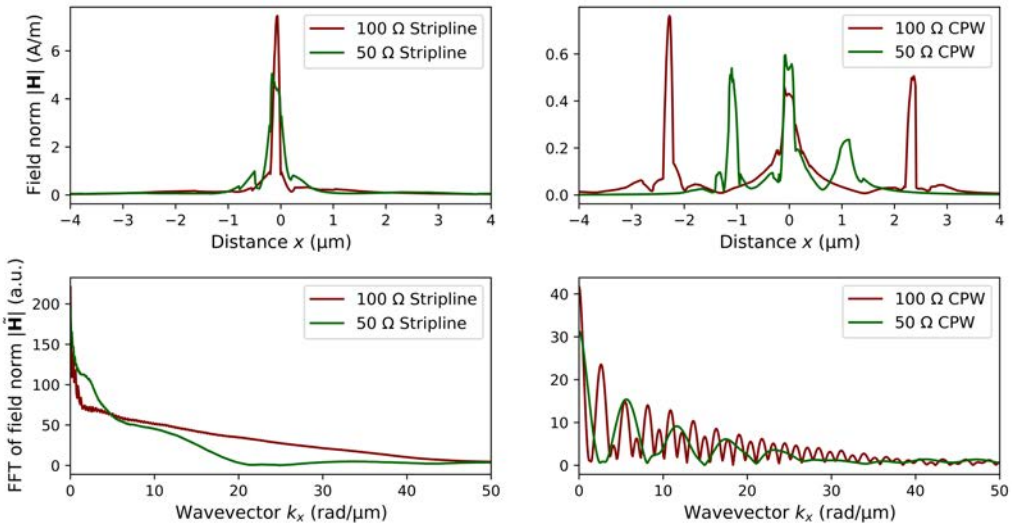

Figure 18: Norm of the magnetic field in a cross sectional plot for the 50 Ω stripline and 100 Ω antennas and the 50 Ω CPW and 100 Ω antennas in the upper plots. Additional, the corresponding FFT of the magnetic field norm for the four different antennas in the lower plots.

port. For a perfect short-circuited transmission with no EM signal radiated into free space $S_{11} = 0\,\text{dB}$ should hold [46]. The results in Figure 20 indicate a low radiation of all four structures, because $S_{11} \approx 0\,\text{dB}$ almost all the EM signal is reflected and the S_{21} parameters are below the experimentally measurable threshold of $-80\,\text{dB}$. The peaks in the S_{11}-parameter originate from resonances in the structures, but are not of significance because they are in the order of 0.02 dB.

Note, to improve the accuracy of the results, the size of the simulation box could be increased, particularly the air domain. If the wavelength is much larger than the dimensions of the simulated structures, the electromagnetic wave may not propagate through the simulation box. However, if the surrounding air domain is of a size equal to or greater than the wavelength of the EM wave, this issue can be overcome.

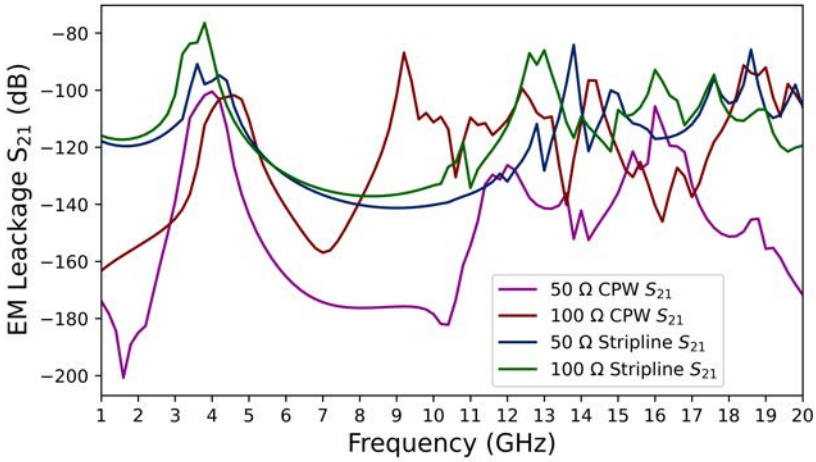

Figure 19: S_{21} parameter in dB-scale of the simulated antenna designs, representing the electromagnetic leakage.

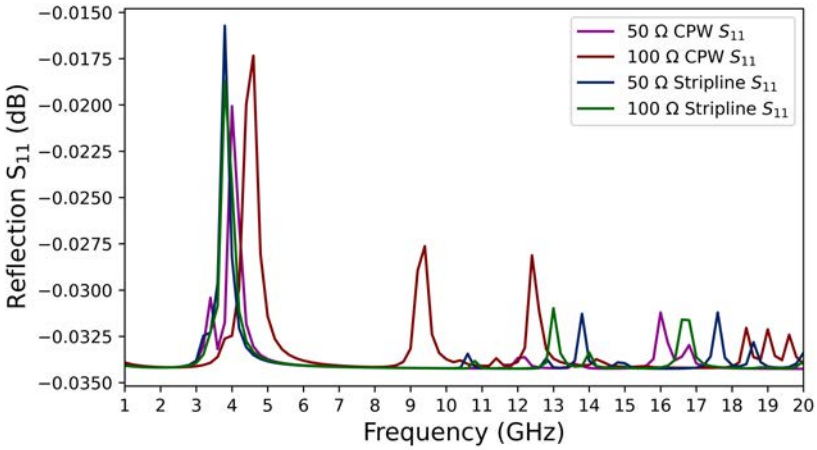

Figure 20: S_{11} parameter in dB-scale of the simulated antenna designs, representing the ratio between the input signal power and the reflected signal power.

2.4.3 Spin-wave dispersion relation

When performing the micromagnetic simulation, the z-component of the magnetisation is saved as a tensor for every time step and every grid point that is on a line along the length of the simulation box. An FFT is applied to this tensor, to transform the quantities time and space into frequency and wavevector. The transformed tensor is plotted in a colour-scale and shows the SW dispersion relation for this specific simulation. Because the effective width of the simulation box is finite at 40 µm, it is not a thin film but rather a broad YIG waveguide. Therefore, to check if the dispersion relation is similar to a thin film it is compared to a thin film simulation obtained from *TetraX*. In Figure 21 the dispersion relation for the simulated YIG waveguide with the excitation field from the 100 Ω stripline antenna conducted by *Magnum.np*, represented by the line of lighter hue in the colour-scale, is compared to the *TetraX* simulation of a YIG thin film, visualised by the dotted white line. Clearly it can be seen, that the dispersion relations agree almost perfectly, which confirms the accuracy of the *Mangnum.np* simulation.

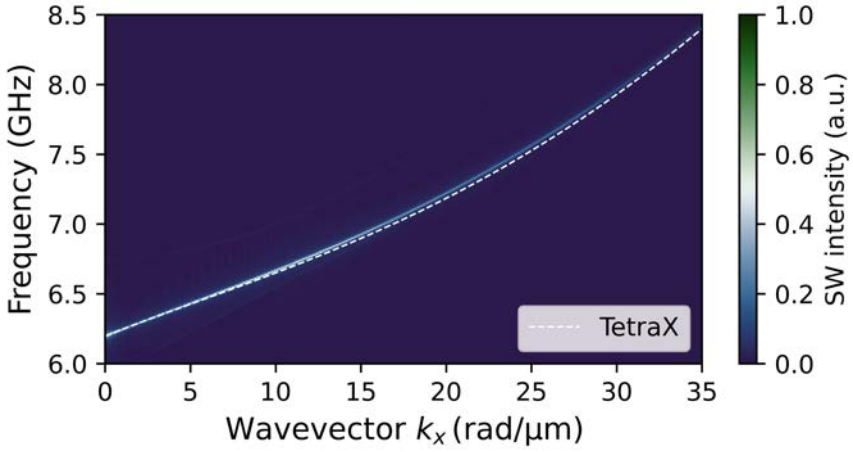

Figure 21: Comparison of dispersion relations obtained by *Magnum.np* represented by the line of lighter hue in the colour-scale and obtained by *TetraX* represented by the dotted white line.

The dispersion relations for the simulations with the imported magnetic fields excited by each of the simulated antennas are displayed in Figure 22. The SW intensity with respect to the frequency of the excitation field is plotted on the left hand side and is calculated by simply summing over all wavevectors values for each frequency value of the colour-scale. The SW intensity is then normalised to have a maximum value of 1. All signals which are below 10 % of the maximum value are filtered out, to reduce computational noise. This causes the left plot to have a clear cut along the zero point on the x-axis as soon as the signal reaches 10 % of maximum. Because the magnetic field distribution was sharper for the 100 Ω stripline antenna than for the 50 Ω stripline antenna, the antenna can excite a far broader spectrum of wavevectors, as predicted and discussed in Section 2.4.1. Figure 22 shows that the distinct modes excited by the CPW antennas for the 50 Ω CPW and 100 Ω CPW antenna fit with the prediction from theory [17].

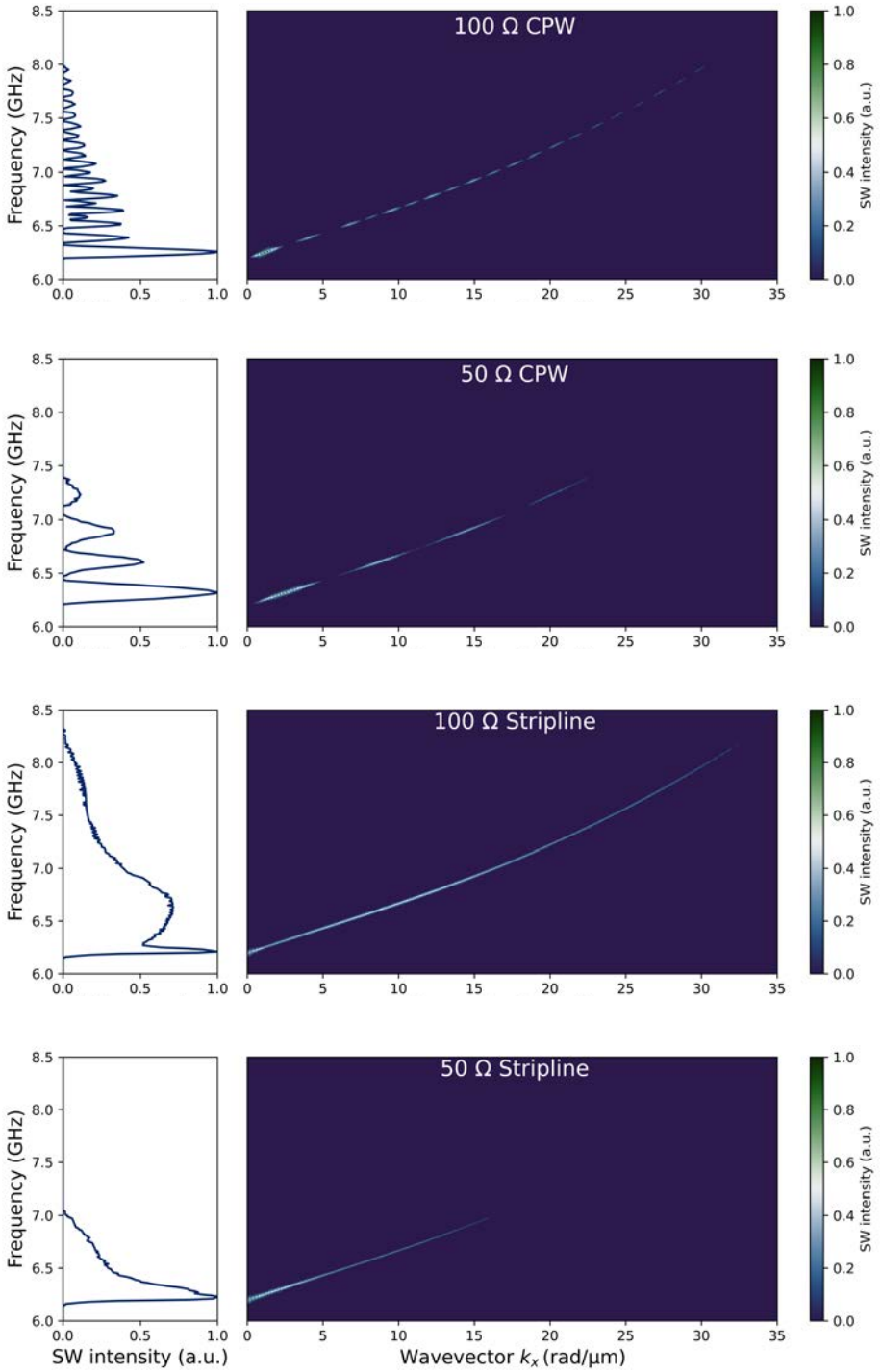

Figure 22: Dispersion relation indicated by the colour-scale and the SW intensity with respect to the excitation frequency. The micromagnetic simulations were performed at a static external field of $H_{\text{stat}} = 150\,\text{mT}$.

3 Sample fabrication

The antennas, which were previously analysed through simulation, have now been fabricated for experimental testing. The process of fabricating structures with sizes as small as 200 nm involves several steps. These steps will be explained in detail in this section. The fabrication took place in the ISO 5 cleanroom facilities of the Central European Institute for Technology (CEITEC), located in the city of Brno, Czech Republic.

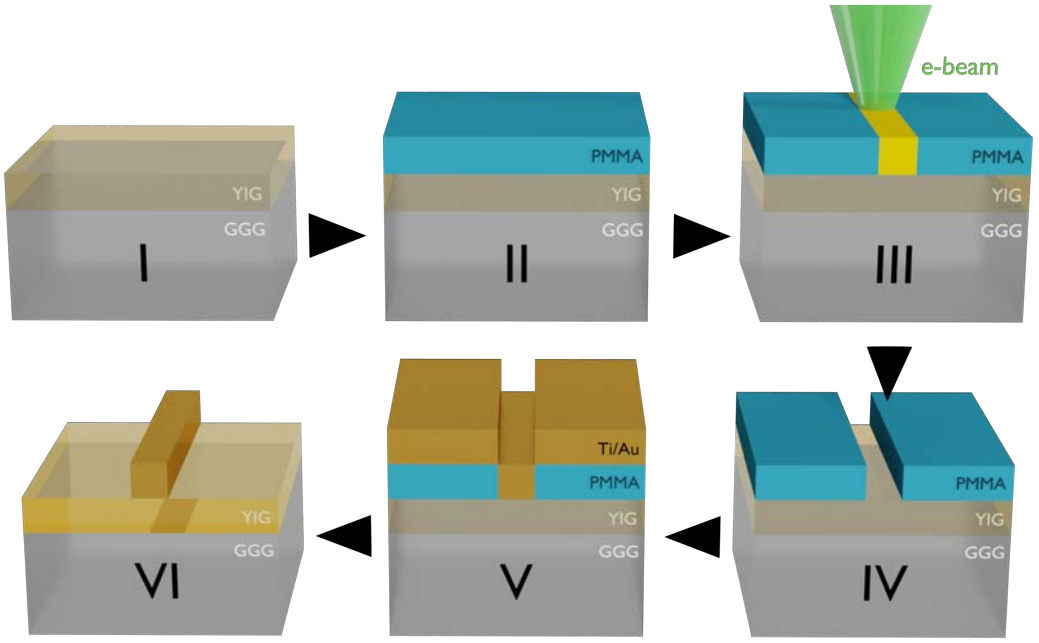

Figure 23: Antenna fabrication: (I) Sample preparation and cleaning, (II) spin coating of PMMA electron beam resist, (III) electron beam lithography, (IV) development PMMA resist, (V) thin film metal deposition, (VI) lift-off process, electron beam exposed regions remain as metallic structure on the sample.

3.1 Sample preparation

As a material to fabricate the nano-antennas on I used 100 nm thick YIG on 500 µm thick GGG. The samples were cut in rectangles of 7×8 mm size. The YIG surface is reduced to a thickness of 48 nm using ion-beam etching. In general, a YIG-GGG sample has a yellowish appearance and is transparent, making it difficult to distinguish between the YIG and GGG surfaces. The samples are therefore marked with a blue dot on the GGG side when they were grown with LPE by our collaborator Carsten Dubs from *INNOVENT e. V. Technologieentwicklung* in Jena, Germany. Because the sample is cleaned in several liquids which would dissolve the colour pigments of the blue dot, I scratched a cross on the GGG side, to distinguish the different surfaces. The next step consists of a cleaning process in two beakers filled with acetone and isopropyl alcohol (IPA) respectively. First the sample is placed in acetone to dissolve contamination and then it is placed in IPA to dissolve the remaining acetone on the sample. The beakers containing the sample is placed in the ultra-sonic cleaner *Elmasonic P* for 10 minutes each, with a frequency of 80 kHz and the power set to 100 % of the maximum power possible by the ultra sonic cleaner.

3.2 Spin coating

In the next step I spin coated layers of polymethylmethacrylate (PMMA) resist, which is the industry standard electron beam resist, on the sample to create a thin layer of electron beam resist for the electron beam lithogrophy. All chemicals used in the spin coating process are produced by the company *Allresist GmbH*. Before the layers of PMMA a layer of adhesion promoter (AR 300-80) is spin coated and the sample is heated to 180 °C for 2 min on the hotplate to increase the adhesion of the PMMA on the sample. Afterwards, two layers of PMMA electron beam resists (AR-P 649.04, AR-P 639.04) with different thicknesses are coated and heated to 150 °C for 3 min. YIG is an electrical insulator and the process of electron beam lithography (EBL) needs an electrically conductive material to avoid electron beam charges to build up on the substrate [47]. Therefore, I used Electra92 (AR-PC 5092), which creates a thin conductive layer for the dissipation of electron beam charges above insulating substrates. It is coated on the sample as the last layer and heated to 90 °C for 2 min.

3.3 Electron beam lithography

A negative lithography mask is created directly on the sample surface by writing patterns in a resist using a focused electron beam (e-beam). The process is based on a change in the chemical properties of the resist when exposed to the electron beam. In a subsequent development step, the resist can be removed in two different ways: either the exposed resist (positive-tone process) or the unexposed resist (negative-tone process) is removed during the development step with a solvent [47]. In this work, I performed a positive-tone process, therefore a positive electron beam resist is used. The used EBL writer is the *Raith150 Two* from the company *Raith GmbH*, which is able to expose patterns with sizes down to 5 nm [48]. To define the path of the electron beam, I created a pattern file using the *KLayout GDS2 Editor* software. The file consists of polygons that forms the desired structure. Figure 24 shows a *KLayout* snapshot. The whole design is

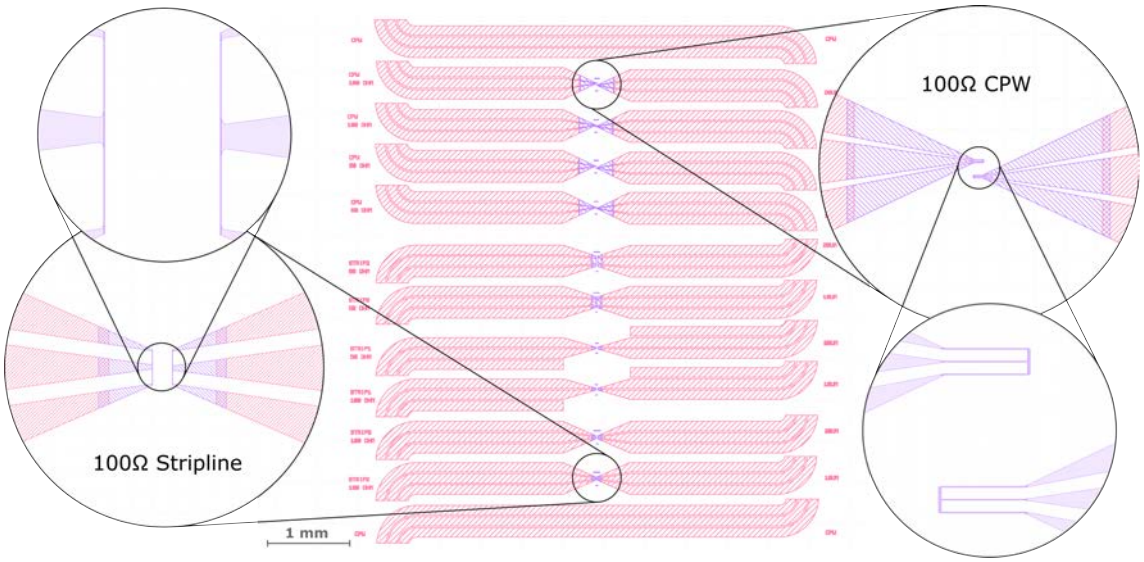

Figure 24: Snapshot of the patterning design using KLayout. Zoom-in on CPW 100 Ω and 100 Ω stripline antenna. Red pattern is lithographed with different electron beam settings than the purple pattern.

separated by two different patterns marked red and purple, which is due to the required accuracy

of different sizes. Therefore, the different patterns are exposed with different e-beam settings. The red, or outer, structure, is larger, ranging from approximately 100 µm to 50 µm lateral size and requires less precision. Therefore, to save patterning time, this structure allows for the use of a larger aperture and higher voltage. An aperture of 120 µm and an acceleration voltage in high voltage mode, which further increases the electron current by a factor of two, of 20 kV is set. These settings results in an electron current of 10.37 nA. The purple, or inner, structure is exposed with an aperture size of 30 µm and a beam voltage of 20 kV with enabled high voltage mode. This setting results in an electron current of 378 pA, which gives a much higher dwell time, but also a much higher resolution, which is necessary as the inner structures range from 50 µm down to 200 nm. The lithography was performed with a working distance of 10 mm, which is the distance between the bottom of the EBL writers column and the sample surface.

3.4 Patterning design

I planned to fabricate five different antenna designs. The antenna pairs were separated by a gap between the outer edge of the antenna for each design of 10 µm and 20 µm, resulting in ten structures. Four of them are similar to the antennas simulated in Section 2, the fifth antenna, referred to as single stripline antenna and visible in Figures 34a and 33a, is similar to the stripline antennas displayed in Figure 29a and 31a. The pads of the stripline 50 Ω and 100 Ω antennas consist of a CPW transmission line with one signal and two ground lines. This design results in two connection lines connecting the signal line with the ground lines. In comparison, the pads of the single stripline antenna consist of only one signal and one ground line, resulting in one connection line, namely one stripline antenna for the whole structure. The patterning file design generally follows the antenna geometry simulated in section 2 but differs in the pad length and ends. Firstly, the length of the pads is longer, with 1.8 mm compared to 1 mm in the simulation. This is due to the fact that the antennas might be used in future experiments in the research group of Nanomagnetism and Magnonics at the University of Vienna. In our cryogenic experiments we connect our samples with bonding wires to the rest of the laboratory setup [11]. When bonding the wires to the pads, a minimum length of pad is required to ensure a good bond, which requires lengthening of the pads. Secondly, the endings of the pads have a 90° curve, as shown in Figure 24. Figures 17 and 24 shows that the direction of spin-wave propagation from the exciting to the detecting antenna, is rotated by 90° for the CPW antennas with respect to the stripline antennas. Thus, it is required to turn the sample, when switching from one antenna type to the other, to ensure the same spin-wave mode excitation, since the external magnetic field axes, and the side from which the pads are connected to the remaining setup, are fixed due to the experimental setup. Additionally, I placed two CPW transmission lines on the outer edges of the sample, to measure the transmission of the experimental setup as a reference signal. Moreover, in Figure 24 that the polygons overlap in the interface region, to ensure a safe connection between them. Because the writing mode is set to longitudinal mode, which drives the beam along the longest length of the currently exposed polygon, the antennas themselves form a separate polygon to let the beam drive along the antenna. Otherwise, if the antenna and the taper would form one united polygon the longest side would be the edge of the taper and the beam would write at an angle to the antenna orientation, which could change the resulting width and decrease the accuracy.

3.5 Resist development

After the EBL, the first step is to remove the thin layer of Electra92 by putting the sample in a beaker filled with deionised water for approximately 1 min. The exposed PMMA resist must then be developed to detach the resist from the sample. Therefore, I placed the sample in a beaker filled with the developer AR 600-56 from *Allresist GmbH* for 3 min. The developed resist was removed from the sample when I put it in the IPA for 30 seconds. A schematic graphic of the sample with the developed resist can be found in Figure 23 (IV).

3.6 Thin-film deposition and lift-off

I applied a 5 nm thick layer of Ti followed by an 85 nm thick layer of Au onto the sample using *Bestec GmbH*'s electron beam evaporator. The reason for depositing a thin layer of Ti first is to enhance the adhesion of the evaporated metallic structure onto the YIG surface. The Au layer is then applied on top of the Ti layer, which serves as a conductor for antenna structures due to its good electronic conductivity and resistance to corrosion. The final step in the fabrication process is to remove all the unexposed PMMA along with the overlying Ti/Au layer. To achieve this, I placed the sample in a beaker filled with acetone overnight. Afterwards, the sample was cleaned in IPA by rinsing away the remaining residuals. The last step in the fabrication process, is to remove all the unexposed PMMA with the overlying Ti/Au layer. Thus, I placed the sample over night in a beaker filled with acetone. Afterwards, I cleaned it in a beaker with IPA.

3.7 Dose test

To maintain the desired lateral sizes by optimising the beam dose parameters, I performed a dose test. Therefore, only the smallest part of the whole structure is fabricated on a small outer region of the sample. Note, that the dose test must not be too close to the edge, as the thickness of the resist changes from the centre to the edge of the sample due to higher a centrifugal force during the spin coating process and therefore the dose required to maintain the same structure size would be different. If the dose test is placed directly at the location where the nano-structures of the overall design would be, the sample would be contaminated with the dose test structures. The positioning of the dose test on the specimen is therefore a compromise between significance and consumption of space on the YIG specimen.

3.8 Sample inspection

Further, I inspected the sample under the optical microscope, and the scanning electron microscope (SEM), to validate the fabrication results and actual antenna dimensions. The images taken of the sample are displayed in Figures 25-34. Further images can be found in the appendix A. Although I designed the antennas to be of 200 nm width, the actual lateral sizes vary between 205.0 nm and 298.0 nm, due to the challenge of fabricating nano-sized structures in general, especially on insulating materials such as YIG. Further, the dimension of the antennas vary depending on the structure design, for instance the mean width of the signal and ground line of the CPW 100 Ω is (275 ± 15) nm, whereas mean width of the lines for the CPW 50 Ω is (248 ± 11) nm. The mean antenna line widths for the 50 Ω and 100 Ω stripline antennas are (225 ± 19) nm and (243 ± 18) nm. The mean lateral size for the single stripline is (238 ± 13) nm. There may be several reasons for the up to 37 % difference between the desired and actual antenna width.

First, the surface of the sample could be of poor quality. Since the sample is etched down from 100 nm to 48 nm thickness of YIG, the surface roughness of the sample can be higher than

on a surface which is created during the LPE process. The etching process could have created an inconsistent surface quality, resulting in defocus of the e-beam on certain regions of the sample because of the surface height variations. In consequence, the actual spot size is bigger when the beam is defocused, resulting in a bigger antenna width.

A second reason could be caused by an inhomogeneous distribution of Electra92. An accumulation of the conducting coating could enhance the dissipation of the electrons at that region, causing the resist to be underdosed, which decreases the depth of exposed resist and can prohibit the deposited metal to get in contact with the substrate. A lack of Electra92 in some regions could increase electron accumulation, because the insulating material can not conduct the electrons away from this point, which increases the electron dose resulting in an overdosed resist and the exposed region is getting bigger in size. This inhomogeneity could be addressed replacing Electra92 by a thin layer of evaporated chromium, which would ensure a more uniform distribution of the conducting layer.

A third reason could be the e-beam current stability. Consequent to possible beam current variation, the electron dose changes for certain exposed structures, yielding a different structural dimension.

Additionally, the spacing between exposed structures may also contribute to writing failures, because of charging and proximity effects, which are more relevant when subsequent writing elements are less far apart, because of the spatial distribution of scattered electrons. While the electrons accumulate at such regions, the PMMA resist is getting overdosed, causing an increase in width [49, 50].

These potential errors may have also contributed to the unsuccessful patterning of the tapers for the antenna depicted in Figure 28 and the poor quality of the antennas in Figures 27 and 30. It can be seen that the antenna is not continuous, as certain segments of the Au structure broke off during the lift-off process. The antennas in Figures 26 and 30 are clearly offset to the taper structure, causing a disconnection between the antenna and the taper. This might be attributed to a possible error of the patterning generator in combination with the longitudinal writing mode of the beam. Figures 33b and 34b show that the distance between the antennas is approximately 20 µm for both structures, although the structure in Figure 34b should be 10 µm apart. This is simply because of a mistake in the patterning file. Additionally, another patterning error is depicted in Figure 35 and may be caused by a discharge of accumulated electrons trough the nonconducting YIG, creating sparks in the YIG thin film, which looks similar to a Lichtenberg Figure [51].

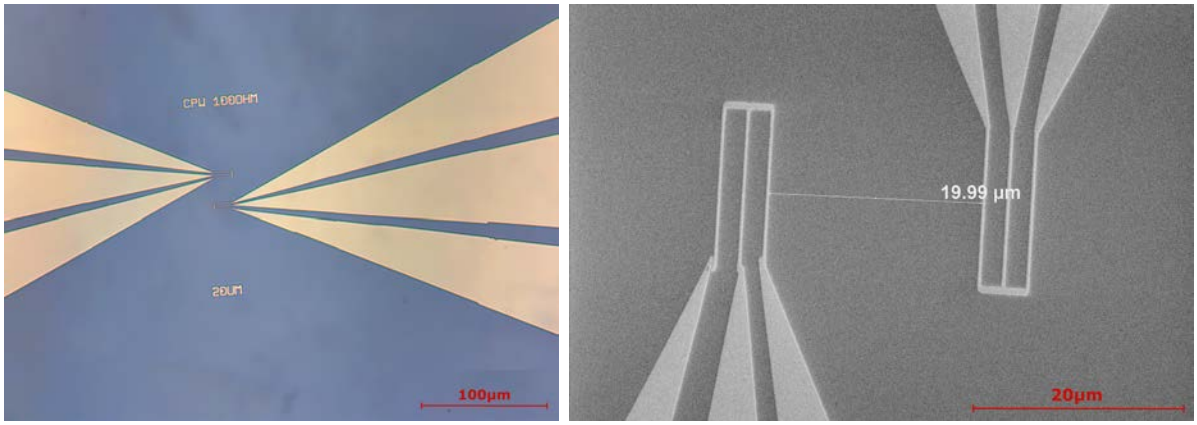

(a) (b)

Figure 25: CPW 100 Ω antennas with a distance of 20 µm between the antennas along the SW propagation direction under the (a) optical microscope and (b) SEM.

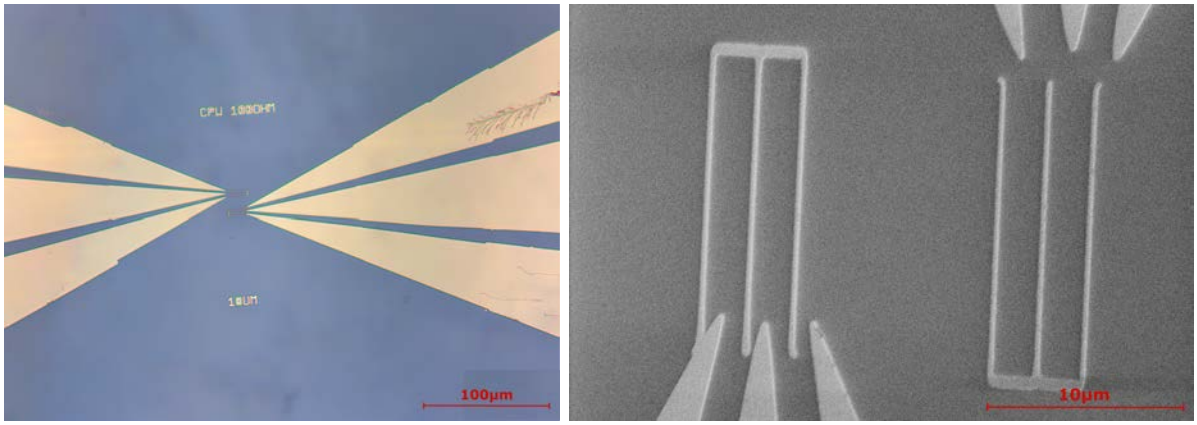

(a) (b)

Figure 26: CPW 100 Ω antennas with a distance of 10 µm between the antennas along the SW propagation direction under the (a) optical microscope and (b) SEM.

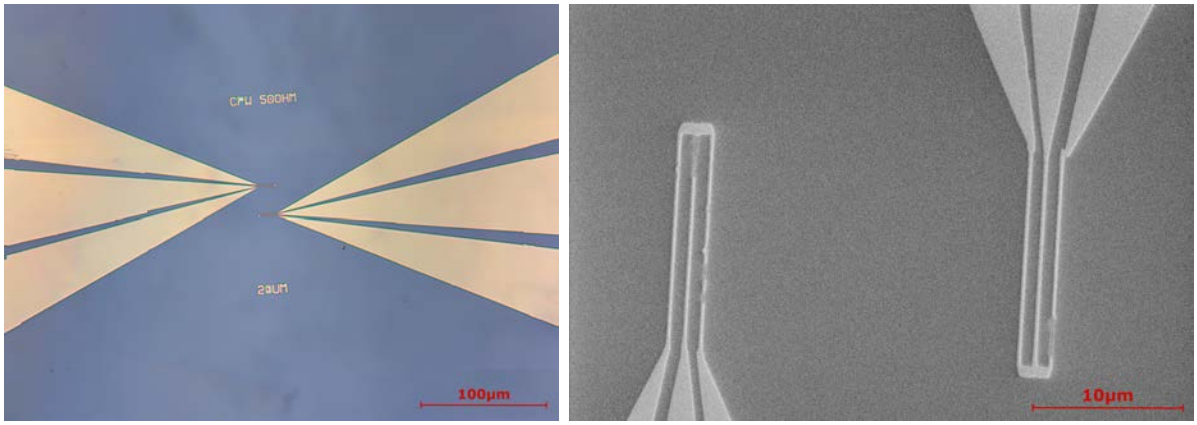

(a) (b)

Figure 27: CPW 50 Ω antennas with a distance of 20 µm between the antennas along the SW propagation direction under the (a) optical microscope and (b) SEM.

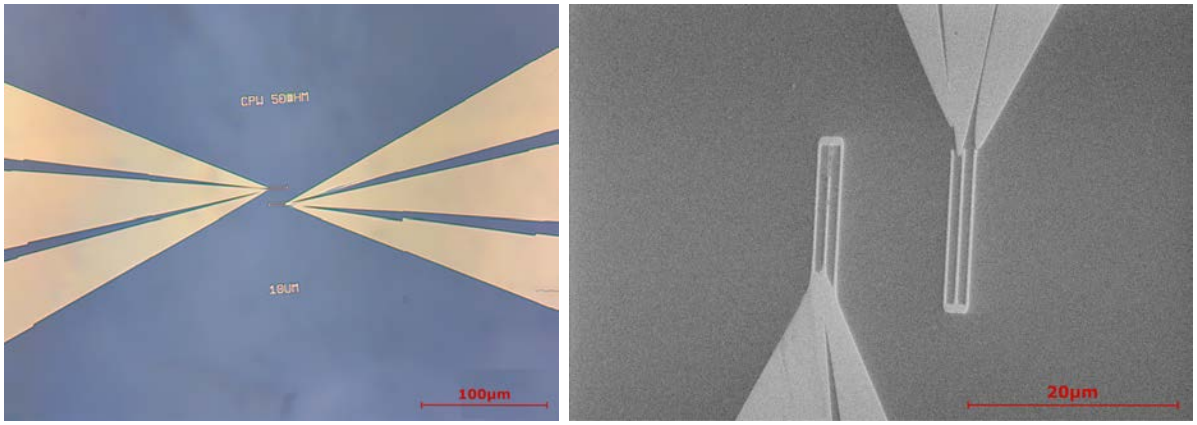

(a) (b)

Figure 28: CPW 50 Ω antennas with a distance of 10 µm between the antennas along the SW propagation direction under the (a) optical microscope and (b) SEM.

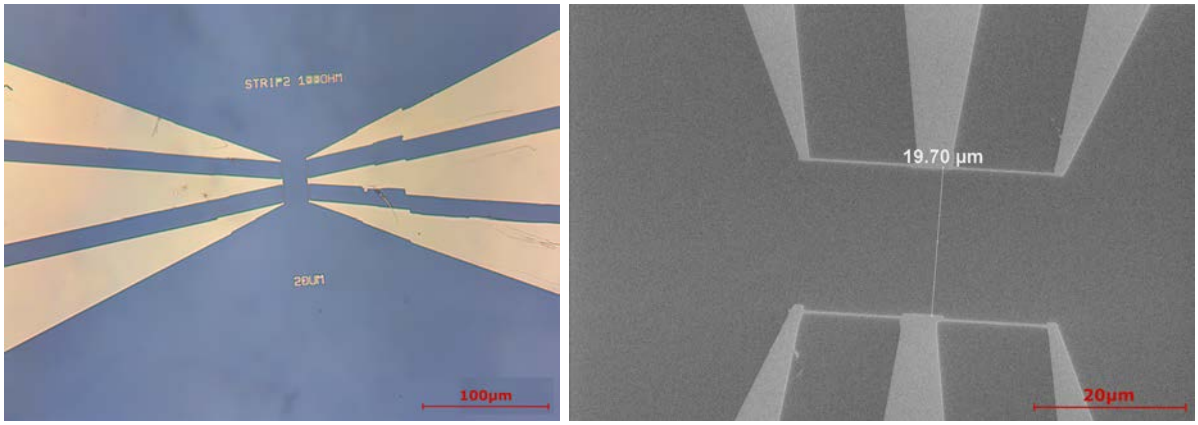

(a) (b)

Figure 29: Stripline 100 Ω antennas with a distance of 20 µm between the antennas along the SW propagation direction under the (a) optical microscope and (b) SEM.

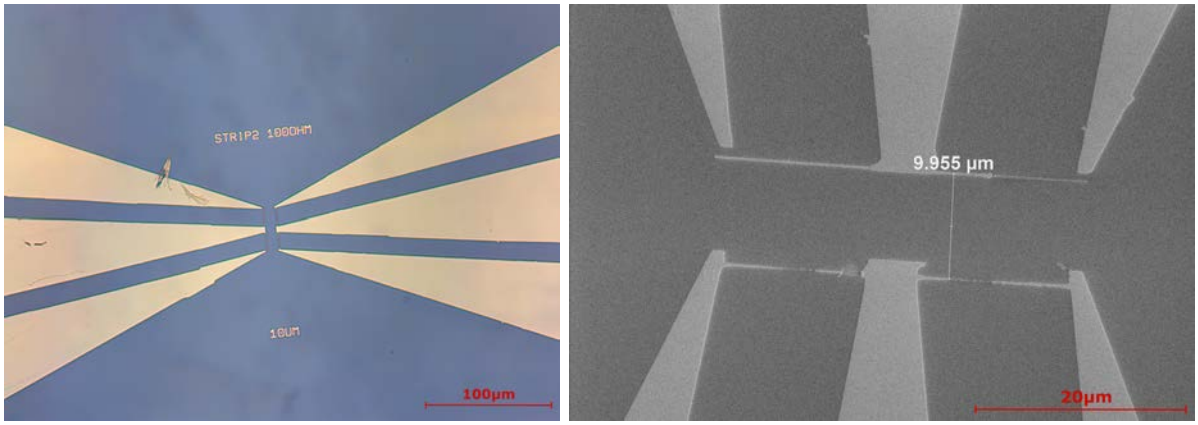

(a) (b)

Figure 30: Stripline 100 Ω antennas with a distance of 10 µm between the antennas along the SW propagation direction under the (a) optical microscope and (b) SEM.

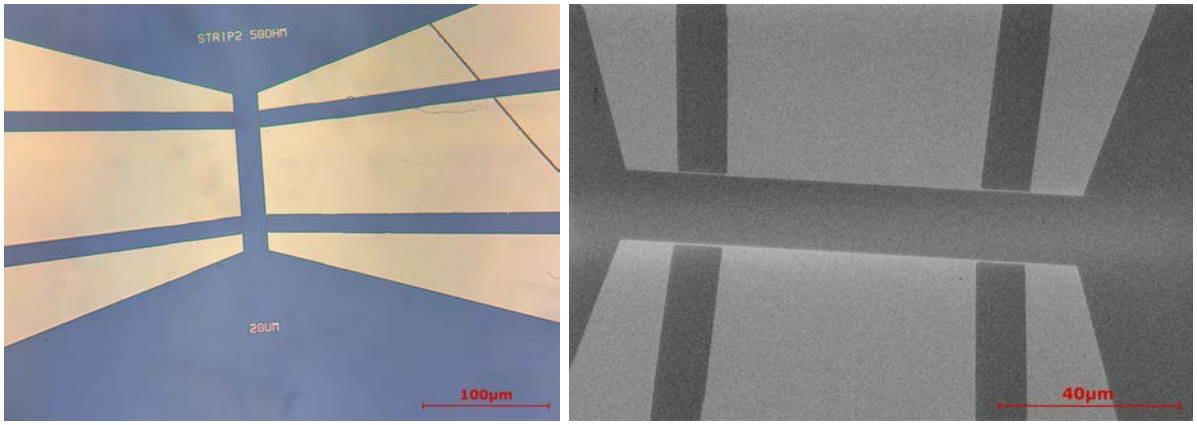

(a) (b)

Figure 31: Stripline 50 Ω antennas with a distance of 20 µm between the antennas along the SW propagation direction under the (a) optical microscope and (b) SEM.

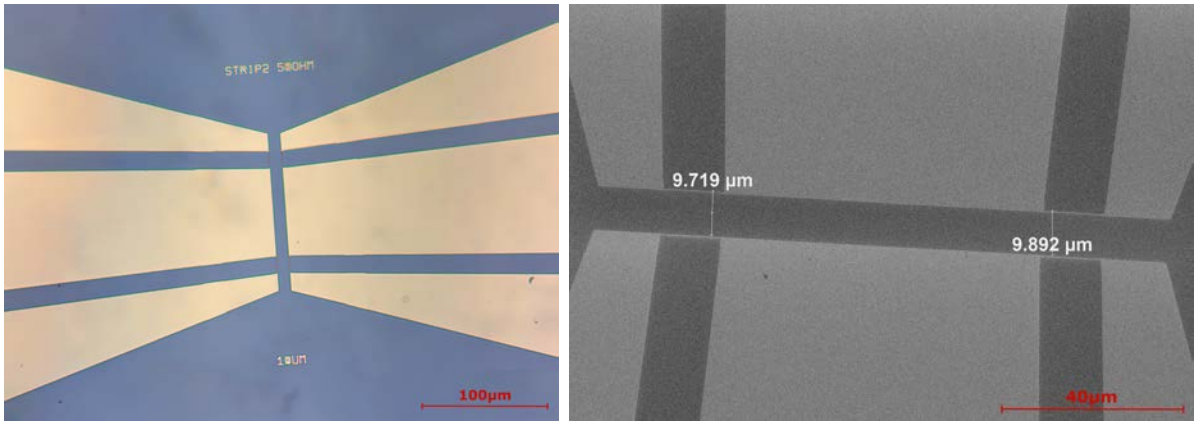

(a) (b)

Figure 32: Stripline 50 Ω antennas with a distance of 10 µm between the antennas along the SW propagation direction under the (a) optical microscope and (b) SEM.

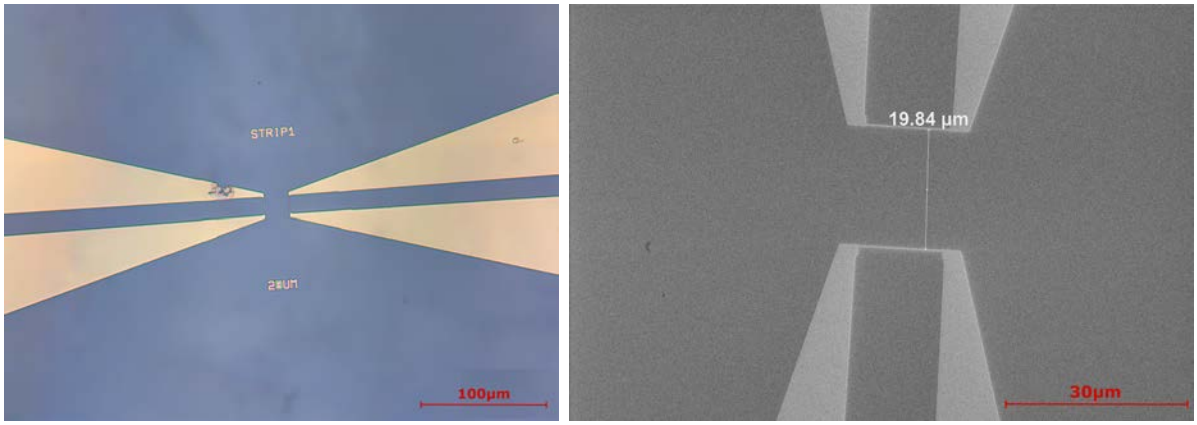

(a) (b)

Figure 33: Single stripline antennas with a distance of 20 µm between the antennas along the SW propagation direction under the (a) optical microscope and (b) SEM.

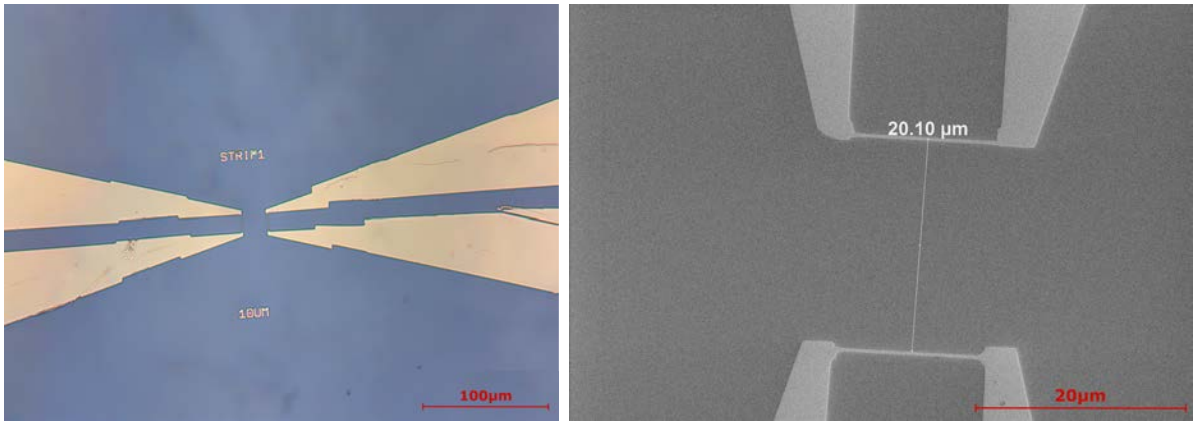

(a) (b)

Figure 34: Single stripline antennas with a distance of 20 µm between the antennas along the SW propagation direction under the (a) optical microscope and (b) SEM.

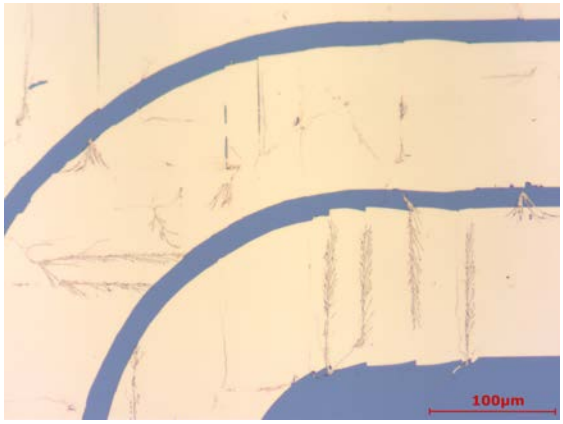

Figure 35: Pads of antenna under the optical microscope, showing an electric discharge resulting in a Lichtenberg figure.

4 All-electrical propagating spin-wave spectroscopy

I used the fabricated antennas to perform AEPSWS at room temperature in the Demon-Eshbach mode configuration. In this section I discuss the results of the AEPSWS and the compare them to theory and numerical simulation results.

4.1 Experimental setup

I conducted the experiments with a high-performance broadband vector network analyser (VNA) from *Anritsu Corporation* model MS4642B, which is highlighted in purple in Figure 36a, and the *GMW* H-frame electromagnet, highlighted in blue in Figure 36a. The VNA has a frequency range of 10 MHz to 20 GHz with a noise floor level of -110 dB. To connect the antennas and the VNA, I utilised high-frequency coaxial cables *Sucoflex 104* in combination with picoprobes from *GGB Industries, Inc.*, model 40A, which can be seen in Figure 37a. I designed and assembled the sample stage on a rail with mounted three-axis-stages where the picoprobes are attached. This movable stage simplifies loading the sample and connecting the picoprobes to the pads. The picoprobes are customised with a 70° bend, as illustrated in Figure 37b, and mounted on three-axis stages. As shown in Figure 37 and the orientation of the structures on the YIG sample in Figure 24, the sample needs to be turned by 90° to achieve the same SW mode configuration (see Figure 3a) for both types of antennas, the stripline, and CPW antennas. Therefore, the pads at the end of the picoprobes have a 90° bend to use the same type of picoprobes for both antennas. To ensure a similar loss at all investigated structures at the bends of the CPW transmission lines, I used the picoprobes with a 70° bend. Picoprobes with a 45° bend would produce the same losses caused by the bends, as the curvature the EM wave has to travel trough the CPW transmission line would be the same for the stripline and CPW antennas. However, such picoprobes were not available in our laboratory. Additionally, to verify the establishment of a connection between the antennas and the picoprobes, I measured the resistance using the DC source meter *Keithley* 2602B. I used the *Anritsu* K251 bias tee to connect the coaxial cable simultaneously with the VNA and the DC source meter.

Figure 36a shows the laboratory setup for measuring all-electrical propagating SW at room temperature. First, the VNA is calibrated manually with the included calibration kit from $1 - 13$ GHz with 16000 measurement points. With the help of the optical microscope (marked yellow in Figure 36a), I guided the picoprobes to the desired antenna pads. The DC source meter is set to resistance measurement mode to ensure sufficient electrical contact with a maximum allowed current of 10 nA to protect the antenna structures. When no connection between pads and picoprobes is made, the resistance equals an open circuit in the range of GOhm to TOhm. However, once an electrical connection was established, the resistance dropped to tens of ohms. If the resistance does not drop down to such values when the picoprobe is in contact with the antenna pads, it has to be assumed that this antenna is broken since no closed circuit was obtained. Note, that the resistance being discussed here is an Ohmic resistance, which is a physical property that is distinct from the characteristic impedance, even though both parameters are measured in Ohms. The measured Ohmic resistances are listed in Table 2 for the 100 Ω CPW, 100 Ω stripline, 50 Ω stripline, and single stripline. Note that the Ohmic resistance vary considerably within a single antenna design. This is likely due to the variation in antenna widths.

For this experiment, I collected reference signals across the entire calibrated frequency range using a -25 dBm port power, and I did not apply any magnetic field. I did not detect any measurable PSWs, and I measured the S_{21} and S_{12} signals as electromagnetic leakage between the antennas with no interaction of SWs since no magnetic field was applied. It's worth noting

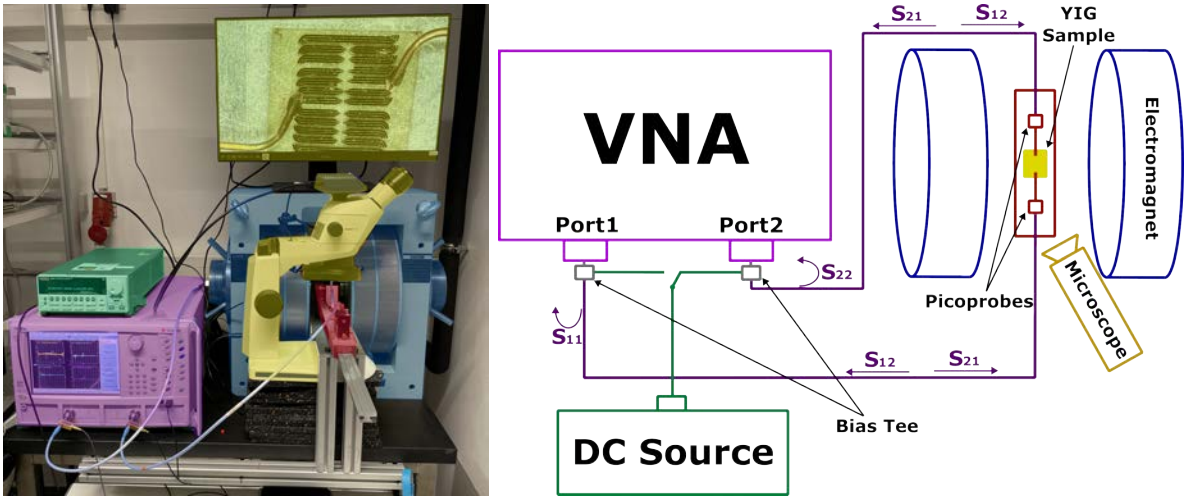

(a) (b)

Figure 36: (a) Photo and (b) a corresponding sketch of the experimental setup for the AEPSWS at room temperature with the VNA (purple), the DC source (green), H-frame electromagnet (blue), optical microscope with a connected monitor to guide the picoprobes mounted on the three-axes-stage (yellow), stage on a rail loaded with the sample, picoprobes and three-axis-stage (red).

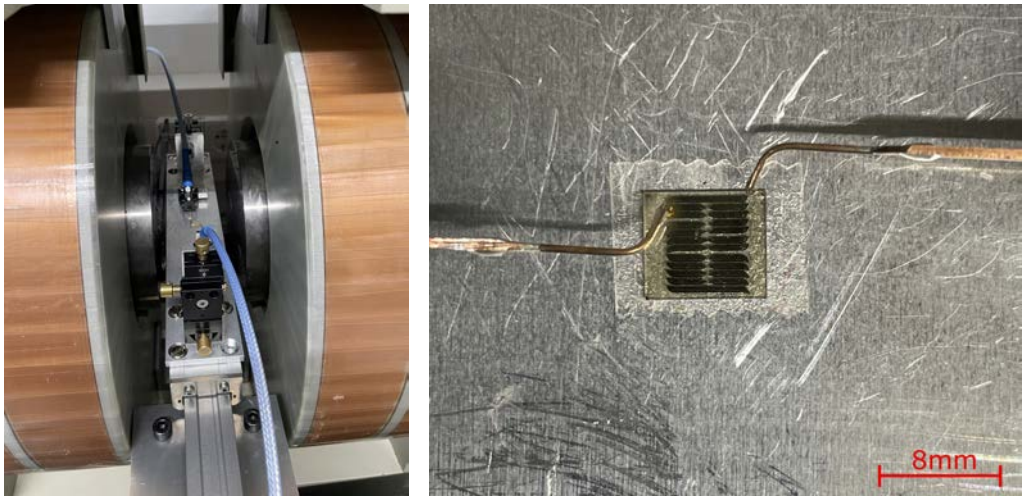

(a) (b)

Figure 37: (a) Sample stage inserted in the middle of the electromagnet. (b) Sample and picoprobes connecting the ends of the CPW reference transmission line of the sample.

that other parts of the setup, such as the picoprobes or the coaxial cables, also contribute to the transmission and reflection of the signal. During data post-processing, I subtracted the reference data from the measured data, both of which are saved in the linear magnitude of the signals' real and imaginary parts.

In Figure 38 the S_{21} coefficients for the measured frequency range are plotted in dB scale for the 100 Ω CPW, 100 Ω stripline and 50 Ω stripline with an antenna gap of 20 µm. It has to be mentioned, that the lower limit of the measurable scattering parameter is around −80 dB for this

Antenna type	Ohmic Resistance (Ω)	
100 Ω CPW	65.0 ± 0.5	101.0 ± 0.5
100 Ω stripline	17.0 ± 0.5	53.0 ± 0.5
50 Ω stripline	28.3 ± 0.5	60.0 ± 0.5
Single stripline	13.4 ± 0.5	72.0 ± 0.5

Table 2: Ohmic resistance of the different measured antennas.

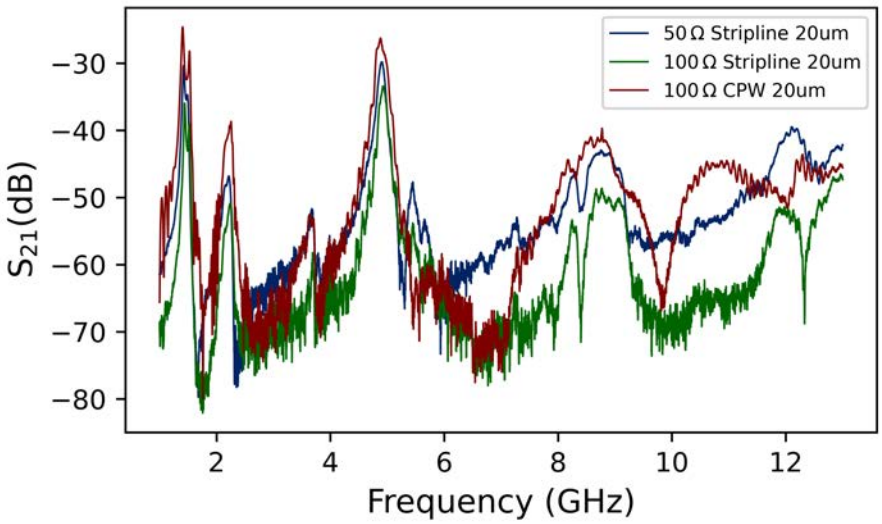

Figure 38: S_{21} coefficient for the CPW 100 Ω, stripline 100 Ω and 50 Ω with an antenna gap of 20 µm, representing the electromagnetic leakage.

experimental setup. This lower limit may be caused by thermal fluctuations, the measurement repeatability of −80 dB given by the picoprobes and the absence of electromagnetic shielding for parts of the setup. Additionally, a little manipulation of the setup, for instance touching the coaxial cables, leads to a relatively high change of the reference signal. For each antenna used for AEPSWS I tuned the electromagnetic field from 25 mT up to 300 mT in 25 mT steps, whereby the field strength of 275 mT and 300 mT forced the sample stage to move, due to a magnetic response of some parts included in the stage. Therefore, this data is not used in the analysis of this thesis because the sample was not placed in the middle of the magnetic poles. The movement of the sample stage altered the magnetic field applied to the sample, and it also shifted the position of the cables, consequently affecting the reference signal.

To fine-tune the magnetic field of the electromagnet, a Hall probe is positioned between the magnetic poles at the same height as the sample to ensure an equivalent radial position. This probe measures the magnetic field and provides feedback to the electromagnet. Consequently, the electromagnet adjusts the current in the coils to achieve the desired magnetic field strength. It's worth noting that the Hall probe is not aligned at the same longitudinal distance from the poles. Figure 37a illustrates that the probe is mounted on the left pole adjacent to the stage. To identify the exact magnetic field which is actually applied on the sample, I extracted the FMR frequencies from the measurements and compared them to FMR frequencies which I calculated numerically with *TetraX*. A mean shift of the measured FMR frequencies of (-35 ± 10) MHz versus the calculated FMR frequencies was recorded and corrected in the obtained results.

4.2 Experimental comparison of the antennas

The objective of this study was to identify the most effective antenna for coupling EM and SW signals. To achieve this, I tested and verified the efficiency of the antennas that were successfully fabricated, in terms of SW transmission. The 100 Ω CPW, 100 Ω stripline, 50 Ω stripline, and the single stripline antenna with an antenna distance of 20 µm were used to conduct the AEPSWS with an applied RF signal port power of −25 dBm. The SW transmission efficiency refers to the power transmitted from port 1 to port 2, which is carried through the SW signal ΔS_{21}. This is measured with a static magnetic field applied to the sample, and the reference signal $S_{21,\mathrm{ref}}$ is taken when no field is applied and then subtracted

$$\Delta S_{21} = S_{21} - S_{21,\mathrm{ref}}. \tag{35}$$

The VNA data are the real $\mathrm{Re}(S_{21})$ and imaginary $\mathrm{Im}(S_{21})$ part of the RF signal. The reference signal is subtracted from the measured signal for the real $\mathrm{Re}(\Delta S_{21}) = \mathrm{Re}(S_{21}) - \mathrm{Re}(S_{21,\mathrm{ref}})$ and imaginary $\mathrm{Im}(\Delta S_{21}) = \mathrm{Im}(S_{21}) - \mathrm{Im}(S_{21,\mathrm{ref}})$ part respectively. To compare the SW signals of the different antennas, the magnitude, $\mathrm{Mag}(\Delta S_{21}) = \sqrt{\mathrm{Im}(\Delta S_{21})^2 + \mathrm{Re}(\Delta S_{21})^2}$, of the ΔS_{21} parameter of the four used antennas is plotted in Figures 39, 40, 41 and 42 in linear scale for static magnetic field strengths of 50 mT, 100 mT, 150 mT and 200 mT. The data points are connected by a solid line for clarity. The plots for the remaining static field values can be found in the appendix B. The measured ΔS_{21} parameters for the 50 Ω and 100 Ω stripline antennas are divided by two, to get the ratio of power transmitted only by one of the two stripline antennas, i.e. the connection line. Additionally, I measured the signal for the 100 Ω stripline with a different VNA namely, the *Rohde & Schwarz* ZVA40 10 − 40 GHz. Because, the VNA used for the other measurements was unavailable for the experimental setup while it was being used for another experiment. I later measured the 100 Ω stripline antenna again with the *Anritsu* VNA, but no PSW was detected. Most likely the antenna broke in the meantime.

For all magnetic fields, the 100 Ω stripline antenna transmitted the highest signal, with up to 1.2 % transmission carried by the SW signal. The second most efficient antenna was the 100 Ω CPW antenna with transmission coefficient of up to 0.6 %. The single stripline transmitted more signal than the 50 Ω stripline antenna, with transmission coefficients of approximately 0.4 % and 0.2 % respectively for their most efficient excitation frequency.

The antennas show different excitation efficiencies for a number of reasons. First, the shape and size of the antennas, as well as the way they are connected, can affect the way electromagnetic signals are transmitted. According to the numerical calculations (see section 2.4.1), using a 100 Ω stripline antenna could produce a stronger magnetic field around the antenna, which could result in a more efficient transmission of signals. Second, the variation of antenna widths due to fabrication issues could distort the actual SW excitation efficiencies concerning the antenna design. A smaller antenna width would increase the current density, resulting in a higher magnetic field induced by the antenna. Although the 100 Ω stripline antenna is larger in width than the 50 Ω stripline antenna, it shows a better SW excitation efficiency. This behaviour suggests that impedance mismatching plays a larger role in the efficiency of spin wave excitation than a slight deviation in antenna width. Third, a reduction in the ohmic resistance of the antennas could enhance the efficiency of SW transmission, as a lower resistance results in a higher current density, which in turn generates a stronger magnetic field around the antenna. This assumption is in agreement with the results, as the 100 Ω stripline exhibits the lowest resistances and the highest SW transmission.

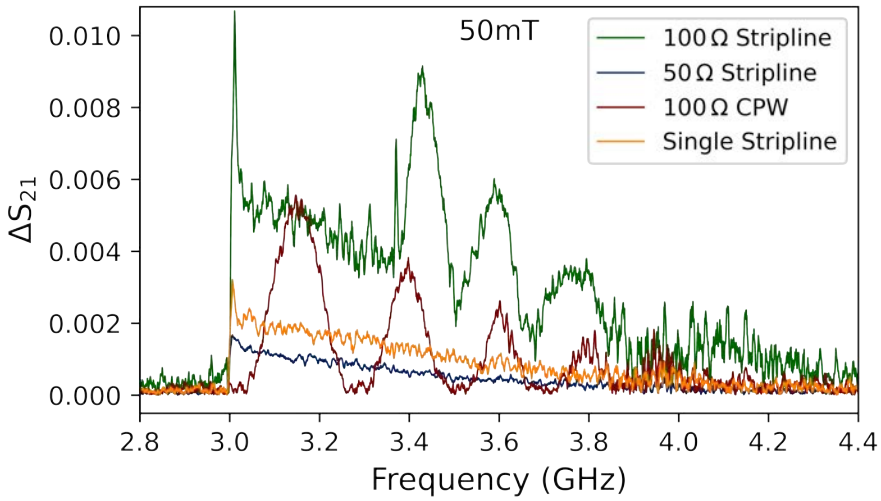

Figure 39: Magnitude of the SW transmission signal ΔS_{21}, for 100 Ω CPW, 100 Ω stripline, 50 Ω stripline and single stripline antenna, at an antenna gap of 20 µm and an applied static magnetic field of 50 mT.

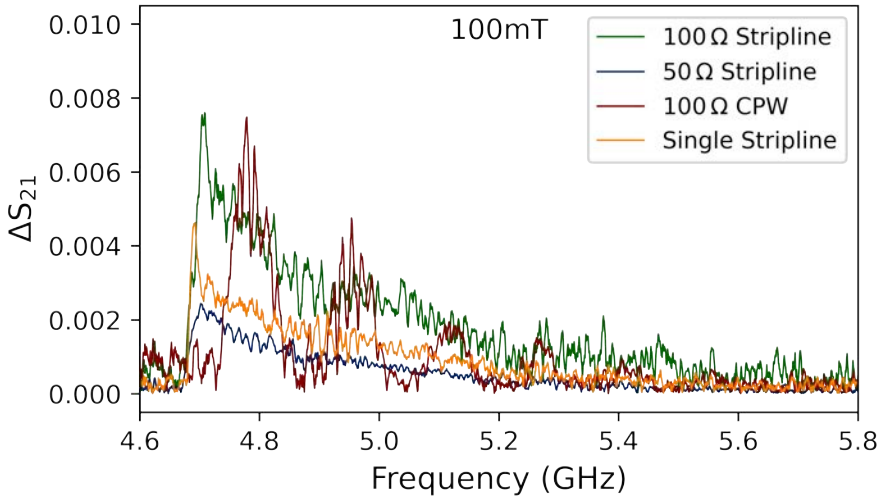

Figure 40: Magnitude of the SW transmission signal ΔS_{21}, for 100 Ω CPW, 100 Ω stripline, 50 Ω stripline and single stripline antenna, at an antenna gap of 20 µm and an applied static magnetic field of 100 mT.

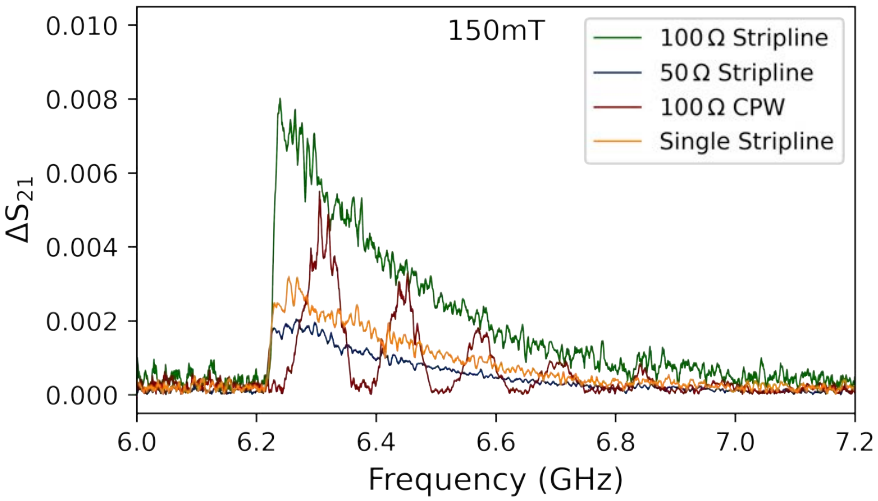

Figure 41: Magnitude of the SW transmission signal ΔS_{21}, for 100 Ω CPW, 100 Ω stripline, 50 Ω stripline and single stripline antenna, at an antenna gap of 20 µm and an applied static magnetic field of 150 mT.

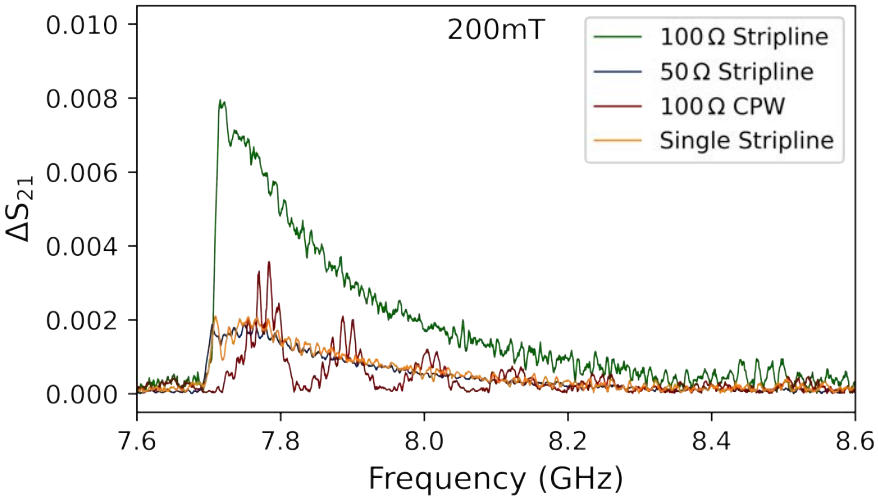

Figure 42: Magnitude of the SW transmission signal ΔS_{21}, for 100 Ω CPW, 100 Ω stripline, 50 Ω stripline and single stripline antenna, at an antenna gap of 20 µm and an applied static magnetic field of 200 mT.

4.3 Comparison of measurement, simulation and theory

In this section I compare the results of experimental measurements, numerical simulations and theoretical calculations in terms of SW transmission for different frequencies. The SW transmission plotted against the frequency for the numerical simulations, is calculated similar like it is described in Section 2.4.3, but instead of *Fourier* transforming the magnetisation $m_z(t, x)$ over the whole length of the FD simulation box, $m_z(t, x)$ is only taken into account in a region of 3 µm around the position of the receiving antenna. The theoretical SW transmission is calculated according to Equation 27. The antenna width for the theoretical current distribution is of 200 nm and distance between ground and signal line for the 100 Ω CPW antenna of 2.1 µm. After Fourier transforming the current distribution, one obtains the SW excitation efficiency with respect to the wavevector k_x, this further transforms into frequency-domain by the use of dispersion relation obtained by the *TetraX* simulation. The frequency range is set from 6.0 GHz to 7.6 GHz for external field strengths of 150 mT and the data points are connected by a solid line, to achieve good visibility of the experimentally measured data. The 100 Ω CPW, 100 Ω stripline and 50 Ω stripline antennas are compared to simulation and theory in this section, given that these antennas were simulated and successfully fabricated.

100 Ω CPW

There is a significant difference between CPW and stripline antennas in their excitation modes. As per the theoretical prediction [52], an antenna can only excite SW wavevectors that correspond to the Fourier transform of the current distribution given by the antenna structure. In the case of CPW antennas, the Fourier transform (depicted in Figure 43 on the right) shows distinct modes that can be excited.

In Figure 43, it is noticeable that the modes do not precisely match the simulations and measurements. This behaviour is because the magnetic field caused by the antenna is not ideally rectangular, as assumed in the theoretical calculations. Looking at Figure 18, we can observe that the signal line's field distribution geometry is Lorentzian, unlike what we assumed to be rectangular. Additionally, the actual magnetic field generated by the antenna is a three-dimensional vector field, which is accounted for in the numerical simulations, unlike the theoretical calculations, which oversimplified it to a one-dimensional vector. As a result, the numerical simulation's SW transmission spectrum agrees with the measurement results. However, the measurement did not observe some additional modes with lower peaks. This deviation can be caused by either finite grid effects, a poor resolution of the magnetic field exported from the finite element electromagnetic simulation compared to the finite difference grid, or reflections of SWs at the edges of the simulation box, even though the edges of the FD box were defined to have a high damping, which should decrease the reflection of SW on the edge of the simulation box.

Additionally, the simulated FMR frequency is shifted by approx. 30 MHz against the measured and theoretically obtained FMR frequency, probably due to some magnetic field aberrations caused by a different sample position in the magnetic field after turning the sample by 90°. The magnetic field offset was only obtained for the 50 Ω stripline and is therefore not ensured to be the same for the CPW antenna.

50 Ω Stripline

The comparison of the measured, simulated and theoretically obtained SW transmission for the 50 Ω stripline is shown in Figure 44. It can be seen that the SW transmission spectrum obtained by simulation is in good agreement with the measured SW transmission spectrum. The

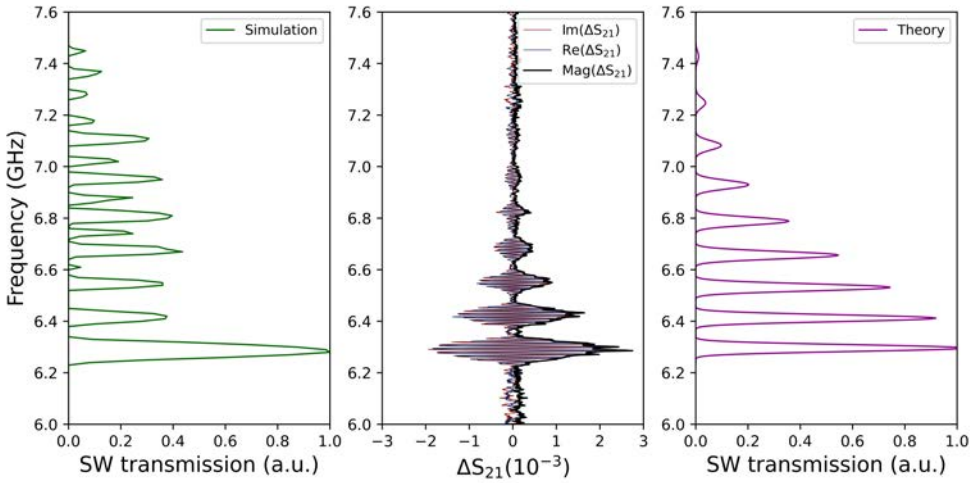

Figure 43: Numerical, experimental and theoretical results for the 100 Ω CPW antenna respectively. Normalised SW transmission efficiency obtained by the numerical simulations (left). Magnitude, imaginary and real part of the ΔS_{21} parameter obtained by AEPSWS with applied static field of 150 mT (centre). Normalised theoretical SW transmission efficiency (right).

theoretical SW transmission spectrum, shown on the right in Figure 44, ends at a frequency of 7.6 GHz, whereas the simulated and measured SW transmission ends between 6.8 GHz and 7.0 GHz. Although, all results take into account SW damping, the simulation and measurement is also limited by a certain noise level, which reduces the maximum detected frequency. Additionally, the shape of the SW transmission spectrum is predicted more accurate by the simulation than by the theoretical calculation.

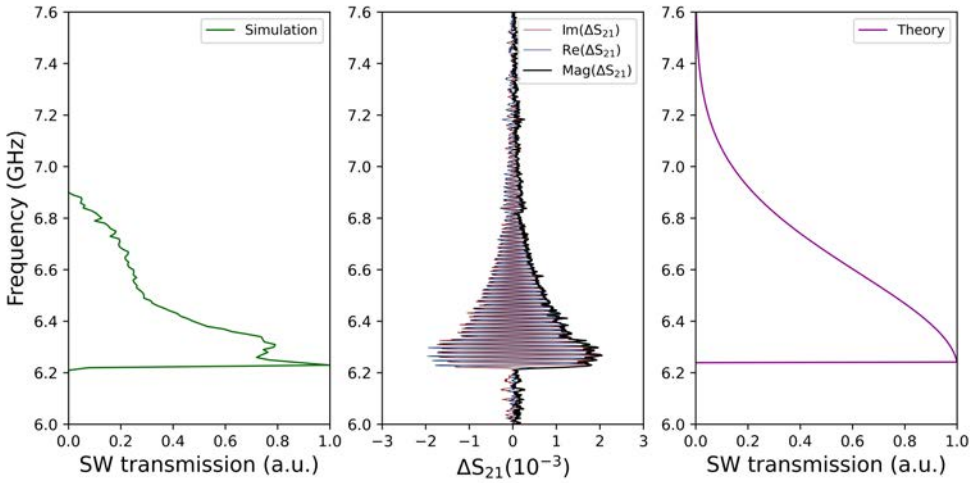

Figure 44: Numerical, experimental and theoretical results for the 50 Ω stripline antenna respectively. Normalised SW transmission efficiency obtained by the numerical simulations (left). Magnitude, imaginary and real part of the ΔS_{21} parameter obtained by AEPSWS with applied static field of 150 mT (centre). Normalised theoretical SW transmission efficiency (right).

100 Ω Stripline

Figure 45 shows the measured, simulated and theoretically calculated SW transmission spectrum for the 100 Ω stripline antenna. It can be seen that the FMR frequency is in agreement within

the measurement, simulation and theory. As the theoretical calculations do not distinguish between the 50 Ω and the 100 Ω stripline antenna, the plot obtained by these calculations in Figure 45 on the right is the same as in Figure 44 on the right. The numerical simulation indicates that the 100 Ω stripline antenna induces a higher magnetic field and a more efficient SW transmission than the other antennas simulated, which is confirmed by the measurements. Although the shape of the SW transmission spectrum do not agree between simulation and measurement, the simulated SW transmission spectrum ranges longer than for the 50 Ω stripline antenna. The abbreviation of the SW transmissions shape is probably caused by computational noise and could be optimised by refining the meshes of the simulations.

In conclusion, the agreement of measurement, simulation and theory proves the usability of these methods for future antenna design. Especially, the frequency range of SW which are possible to excite with an antenna can be modelled accurately. Additionally, the SW intensity at any distance from the excitation antenna can be analysed in a post-processing step. Note, the accuracy of the simulated SW spectrum can be increased by increasing the number of cells and the total simulation time in the micromagnetic simulation. Further improvements could be done by refining the mesh of the electromagnetic simulation, which would resolve the magnetic field distribution created by the antenna more accurately.

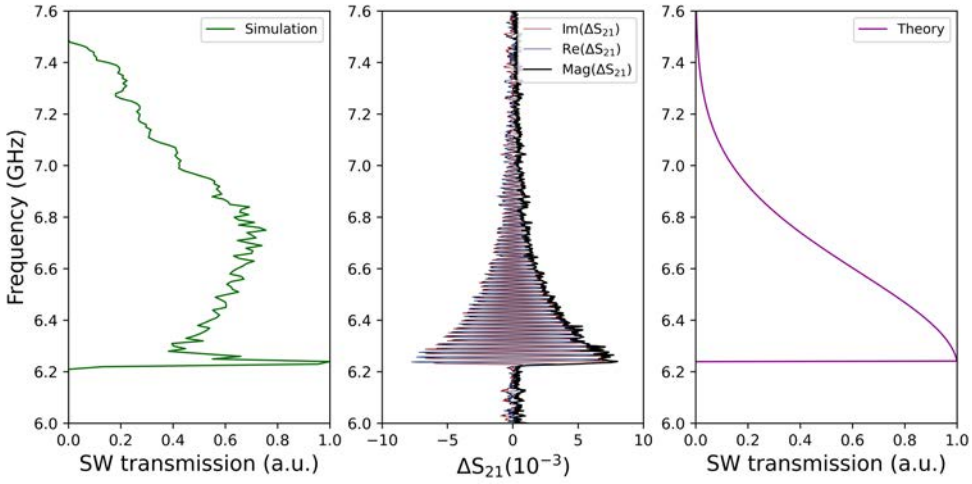

Figure 45: Numerical, experimental and theoretical results for the 100 Ω stripline antenna respectively. Normalised SW transmission efficiency obtained by the numerical simulations (left). Magnitude, imaginary and real part of the ΔS_{21} parameter obtained by AEPSWS with applied static field of 150 mT (centre). Normalised theoretical SW transmission efficiency (right).

4.4 Group velocity

The theoretical group velocity of the propagating SWs in x-direction is the derivative of the dispersion relation, $v_{g,th} = d\omega/dk_x$. In Figure 46 the theoretically, numerically and experimentally obtained group velocities are compared.

The theoretical group velocity, as the derivative of the theoretical dispersion relation obtained by *Kalinikos* and *Slavin* [53], is indicated by the black solid line. The numerically obtained group velocity as the derivative of the dispersion relation obtained by *TetraX*, is plotted with the black dashed line. The experimentally obtained group velocities are shown for the 100 Ω stripline (blue

dots), the 50 Ω stripline (red dots), and CPW 100 Ω (green dots) antenna respectively at an external magnetic field of 50 mT.

The periodicity δf of the oscillations in the Re(S_{21}) parameter is given by a phase delay $\phi = k_x \cdot D$ for a given wavevector k_x and the distance D between the antennas. Assuming a constant group velocity within one period of the oscillation of the Re(S_{21}) parameter, one can insert the phase delay for a full period $\phi = 2\pi$ into the relation $\delta k_x \simeq 2\pi\delta f / v_g$, with δk_x the range of wavevector within a full period of phase delay. So the measured group velocity is given by $v_{g,exp} = \delta f \cdot D$, with δf the periodicity of the oscillations in the Re(S_{21}) parameter and D the distance between the antennas [17]. The saturation magnetisation is fitted to $M_s = 144 \times 10^3$ A/m, which is in good agreement with the literature [11, 39, 54].

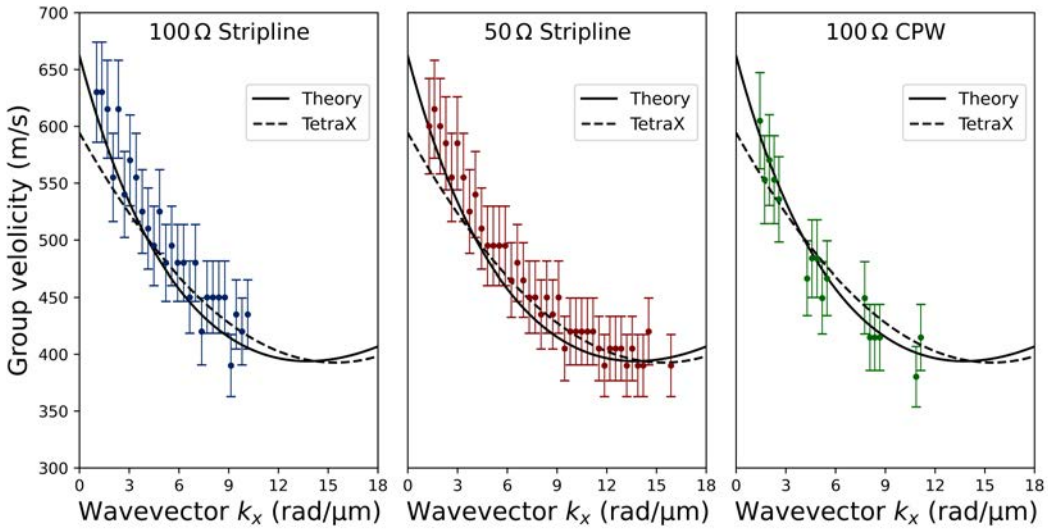

Figure 46: Group velocity of propagating SWs in 48 nm thick YIG film at an external field of 50 mT. Theoretical group velocity obtained by the derivative of the theoretical dispersion relation (black solid line), numerical group velocity as the derivative of the dispersion relation obtained by *TetraX* (black dashed line), and experimentally obtained group velocities for the the 100 Ω stripline antenna (blue dots), the 50 Ω stripline antenna (red dots), and CPW 100 Ω antenna (green dots).

Predicted by simulation and theory the CPW antenna has distinct modes which can be excited, resulting in missing values for the group velocity between these modes. The errors in measured group velocities were estimated based on frequency resolution. As the group velocity is independent of antenna design, the measured values fit the theoretical and numerical curve equally well.

5 Conclusion and Outlook

In my thesis, I utilised a combination of electromagnetic and micromagnetic simulation techniques to describe the coupling of microwave and micromagnetic signals in a numeric regime using only Maxwell's equations and the LLG equation. The study evaluated the SW spectrum excitation efficiency of the antennas. I proved the results experimentally with example fabricated and measured sub-micrometer on-chip lithographed antennas for SW excitation and detection. Until this work, it has not been demonstrated to convert from finite difference to finite element methods, and therefore, gaining insight into the complete treatment of the problem, from the excitation of an RF signal in the antenna to the propagating spin wave.

The SW dispersion relation obtained from the numerical simulations using *Magnum.np* agrees with the SW dispersion relation for a YIG thin film obtained using the micromagnetic modelling package *TetraX*. The simulated SW spectrum of the different antennas are in agreement with the measurement results, proving the utility of these methods for future antenna designs concerning a specifically tailored SW excitation and detection spectrum. Note, the simulation can be extended by transferring every time step from the electromagnetic simulation into the micromagnetic simulation. This would allow for new investigation possibilities, such as analysing how complex-shaped pulses excited in antennas will transfer into spin-wave pulses. It has been observed that the conducted simulations need improvements for greater precision. For instance, systematic studies are necessary to obtain the optimum mesh size that minimises computing time and maximises accuracy.

Further, I successfully fabricated Ti/Au structures with lateral sizes down to 225 nm on insulating YIG using electron-beam lithography combined with physical vapour deposition. The 100 Ω stripline, 50 Ω stripline, single stripline, and 100 Ω CPW antennas were successfully fabricated and used for all-electrical propagating spin-wave spectroscopy. The fabrication process revealed, that possible charging effects on the insulating sample used for e-beam lithography may have overdosed the resist or destroyed regions of the substrate material. Future research will determine if the conducting layer Electra92 coated on the sample would be better replaced by a thin layer of evaporated chromium, which would ensure a more uniform distribution of the conducting layer. I also experienced difficulties with the exact positioning of different polygon structures within one write field, leading to an unsuccessful connection between antennas and tapers. This may originated from a possible error of the patterning generator in combination with the longitudinal writing mode of the beam, which could be solved by fixing the writing direction of the beam to one axis, preferably the axis along the antenna length. Additionally, the decrease in the antennas' width and thickness could increase the SW excitation efficiency, as a result of increasing current density, which leads to a higher local magnetic field induced by the antenna. Nanofabrication on YIG samples faces challenges in reducing sizes, making it a challenging topic for future research, although, antennas with lateral sizes of 125 nm, for a broadband SW excitation, has already been realised by Ciubotaro *et al.* [14].

Using the fabricated antennas, I performed all-electrical propagating spin-wave spectroscopy up to 250 mT external field. The measured group velocities of the propagating SWs, up to 630 m/s, are in agreement with the theoretically calculated group velocities. I have shown that the 100 Ω stripline antenna has achieved a power transmission ratio of up to 1.2 % for a propagation length of 20 µm in a 48 nm thick YIG film. It has been observed that the stripline antenna with an impedance of 100 Ω induces a stronger magnetic field in the YIG film compared to the stripline antenna with 50 Ω. Furthermore, it transmits more power through the SW signal between the antennas. This finding is consistent with the hypothesis that a higher impedance in a short-circuited transmission line, when compared to the remaining structures and setup,

results in higher induced magnetic field. Furthermore, this result corroborates the assumption that a reduction in Ohmic resistance could enhance the efficiency of SW transmission. Using the methods developed in this thesis, future investigations will determine the characteristic impedance of antennas, including their design, at which the optimum SW excitation can be achieved.

In conclusion, this thesis presents a combination of finite element electromagnetic and finite difference micromagnetic simulations of sub-micrometre antennas for SW excitation and detection. The simulated results were confirmed by fabricating and measuring the antennas, performing all-electrical propagating spin-wave spectroscopy.

References

[1] A. V. Chumak, V. I. Vasyuchka, A. A. Serga, and B. Hillebrands, "Magnon spintronics," *Nature Physics*, vol. 11, pp. 453–461, 2015.

[2] A. V. Chumak, P. Kabos, M. Wu, C. Abert, C. Adelmann, A. O. Adeyeye, J. Åkerman, F. G. Aliev, A. Anane, A. Awad, C. H. Back, A. Barman, G. E. W. Bauer, M. Becherer, E. N. Beginin, V. A. S. V. Bittencourt, Y. M. Blanter, P. Bortolotti, I. Boventer, D. A. Bozhko, S. A. Bunyaev, J. J. Carmiggelt, R. R. Cheenikundil, F. Ciubotaru, S. Cotofana, G. Csaba, O. V. Dobrovolskiy, C. Dubs, M. Elyasi, K. G. Fripp, H. Fulara, I. A. Golovchanskiy, C. Gonzalez-Ballestero, P. Graczyk, D. Grundler, P. Gruszecki, G. Gubbiotti, K. Guslienko, A. Haldar, S. Hamdioui, R. Hertel, B. Hillebrands, T. Hioki, A. Houshang, C.-M. Hu, H. Huebl, M. Huth, E. Iacocca, M. B. Jungfleisch, G. N. Kakazei, A. Khitun, R. Khymyn, T. Kikkawa, M. Kläui, O. Klein, J. W. Kłos, S. Knauer, S. Koraltan, M. Kostylev, M. Krawczyk, I. N. Krivorotov, V. V. Kruglyak, D. Lachance-Quirion, S. Ladak, R. Lebrun, Y. Li, M. Lindner, R. Macêdo, S. Mayr, G. A. Melkov, S. Mieszczak, Y. Nakamura, H. T. Nembach, A. A. Nikitin, S. A. Nikitov, V. Novosad, J. A. Otálora, Y. Otani, A. Papp, B. Pigeau, P. Pirro, W. Porod, F. Porrati, H. Qin, B. Rana, T. Reimann, F. Riente, O. Romero-Isart, A. Ross, A. V. Sadovnikov, A. R. Safin, E. Saitoh, G. Schmidt, H. Schultheiss, K. Schultheiss, A. A. Serga, S. Sharma, J. M. Shaw, D. Suess, O. Surzhenko, K. Szulc, T. Taniguchi, M. Urbánek, K. Usami, A. B. Ustinov, T. van der Sar, S. van Dijken, V. I. Vasyuchka, R. Verba, S. V. Kusminskiy, Q. Wang, M. Weides, M. Weiler, S. Wintz, S. P. Wolski, and X. Zhang, "Advances in magnetics roadmap on spin-wave computing," *IEEE Transactions on Magnetics*, vol. 58, pp. 1–72, 2022.

[3] Q. Wang, G. Csaba, R. Verba, A. V. Chumak, and P. Pirro, "Perspective on nanoscaled magnonic networks," *arXiv:2311.06129 [physics.app-ph]*, 2023.

[4] A. A. Serga, A. V. Chumak, and B. Hillebrands, "Yig magnonics," *Journal of Physics D: Applied Physics*, vol. 43, 2010.

[5] B. Heinz, T. Brächer, M. Schneider, Q. Wang, B. Lägel, A. M. Friedel, D. Breitbach, S. Steinert, T. Meyer, M. Kewenig, C. Dubs, P. Pirro, and A. V. Chumak, "Propagation of spin-wave packets in individual nanosized yttrium iron garnet magnonic conduits," *Nano Letters*, vol. 20, pp. 4220–4227, 2020.

[6] Q. Wang, M. Kewenig, M. Schneider, R. Verba, F. Kohl, B. Heinz, M. Geilen, M. Mohseni, B. Lägel, F. Ciubotaru, C. Adelmann, C. Dubs, S. D. Cotofana, O. V. Dobrovolskiy, T. Brächer, P. Pirro, and A. V. Chumak, "A magnonic directional coupler for integrated magnonic half-adders," *Nature Electronics*, vol. 3, pp. 765–774, 2020.

[7] G. Talmelli, T. Devolder, N. Träger, J. Förster, S. Wintz, M. Weigand, H. Stoll, M. Heyns, G. Schütz, I. P. Radu, J. Gräfe, F. Ciubotaru, and C. Adelmann, "Reconfigurable submicrometer spin-wave majority gate with electrical transducers," *Sci. Adv*, vol. 6, pp. 4042–4060, 2020.

[8] M. Schneider, D. Breitbach, R. O. Serha, Q. Wang, A. A. Serga, A. N. Slavin, V. S. Tiberkevich, B. Heinz, B. Lägel, T. Brächer, C. Dubs, S. Knauer, O. V. Dobrovolskiy, P. Pirro, B. Hillebrands, and A. V. Chumak, "Control of the bose-einstein condensation of magnons by the spin hall effect," *Physical Review Letters*, vol. 127, 2021.

[9] D. Xu, X.-K. Gu, H.-K. Li, Y.-C. Weng, Y.-P. Wang, J. Li, H. Wang, S.-Y. Zhu, and J. Q. You, "Quantum control of a single magnon in a macroscopic spin system," *Physical Review Letters*, vol. 130, p. 193603, May 2023.

[10] R. G. Morris, A. F. V. Loo, S. Kosen, and A. D. Karenowska, "Strong coupling of magnons in a yig sphere to photons in a planar superconducting resonator in the quantum limit," *Scientific Reports*, vol. 7, 2017.

[11] S. Knauer, K. Davídková, D. Schmoll, R. O. Serha, A. Voronov, Q. Wang, R. Verba, O. V. Dobrovolskiy, M. Lindner, T. Reimann, C. Dubs, M. Urbánek, and A. V. Chumak, "Propagating spin-wave spectroscopy in a liquid-phase epitaxial nanometer-thick yig film at millikelvin temperatures," *Journal of Applied Physics*, vol. 133, 2023.

[12] M. Vaňatka, K. Szulc, O. c. v. Wojewoda, C. Dubs, A. V. Chumak, M. Krawczyk, O. V. Dobrovolskiy, J. W. Kłos, and M. Urbánek, "Spin-wave dispersion measurement by variable-gap propagating spin-wave spectroscopy," *Physical Review Applied*, vol. 16, p. 054033, 2021.

[13] Y. Rao, D. Zhang, L. Jin, Z. Zhong, Q. Yang, M. Li, J. Li, Y. Yang, G. Wang, G. Gan, and H. Zhang, "Antenna design for ferromagnetic resonance and spin wave spectroscopy," *Journal of Magnetism and Magnetic Materials*, vol. 490, p. 165442, 2019.

[14] F. Ciubotaru, T. Devolder, M. Manfrini, C. Adelmann, and I. P. Radu, "All electrical propagating spin wave spectroscopy with broadband wavevector capability," *Applied Physics Letters*, vol. 109, p. 012403, 2016.

[15] Y. Zhang, T. Yu, J. lei Chen, Y. guang Zhang, J. Feng, S. Tu, and H. Yu, "Antenna design for propagating spin wave spectroscopy in ferromagnetic thin films," *Journal of Magnetism and Magnetic Materials*, vol. 450, pp. 24–28, 2018.

[16] K. Mori, T. Goto, T. Watanabe, T. Koguchi, Y. Nakamura, P. B. Lim, A. B. Ustinov, and M. Inoue, "Broadband excitation of spin wave using microstrip line antennas for integrated magnonic devices," *Journal of Physics D: Applied Physics*, vol. 55, p. 115002, 2021.

[17] V. Vlaminck and M. Bailleul, "Spin-wave transduction at the submicrometer scale: Experiment and modeling," *Physical Review B*, vol. 81, p. 014425, 2010.

[18] K. M. Krishnan, *Fundamentals and Applications of Magnetic Materials*. Oxford University Press, 2016.

[19] D. D. Stancil and A. Prabhakar, *Spin Waves, Theory and Applications*. Springer, 1. ed., 2009.

[20] H. A. Mugiraneza, S., "Tutorial: a beginner's guide to interpreting magnetic susceptibility data with the curie-weiss law.," *Commun Phys*, vol. 95, 2022.

[21] A. Aharonî, *Introduction to the theory of ferromagnetism*. Oxford University Press, 2. ed., 2000.

[22] E. Schlömann, "A sum rule concerning the inhomogeneous demagnetizing field in nonellipsoidal samples," *Journal of Applied Physics*, vol. 33, pp. 2825–2826, 1962.

[23] R. I. Joseph and E. Schlömann, "Demagnetizing field in nonellipsoidal bodies," *Journal of Applied Physics*, vol. 36, pp. 1579–1593, 1965.

[24] S. Chikazumi, *Physics of ferromagnetism*. Oxford University Press, 2. ed., 2009.

[25] A. Barman and J. Sinha, *Spin Dynamics and Damping in Ferromagnetic Thin Films and Nanostructures*. Springer, 1. ed., 2018.

[26] R. W. Damon and J. R. Eshbach, "Magnetostatic modes of a ferromagnet slab," *Journal of Physics and Chemistry of Solids*, vol. 19, pp. 308–320, 1961.

[27] C. Dubs, O. Surzhenko, R. Linke, A. Danilewsky, U. Brückner, and J. Dellith, "Sub-micrometer yttrium iron garnet lpe films with low ferromagnetic resonance losses," *Journal of Physics D: Applied Physics*, vol. 50, p. 204005, 2017.

[28] V. Cherepanov, I. Kolokolov, and V. L'vov, "The saga of yig: Spectra, thermodynamics, interaction and relaxation of magnons in a complex magnet," *Physics Reports*, vol. 229, pp. 81–144, 1993.

[29] N. Ibrahim, C. Edwards, and S. Palmer, "Pulsed laser ablation deposition of yttrium iron garnet and cerium-substituted yig films," *Journal of Magnetism and Magnetic Materials*, vol. 220, pp. 183–194, 2000.

[30] "Wikepedia, skin effect." `https://en.wikipedia.org/wiki/Skin_effect`. Accessed: 2023-12-14.

[31] F. Gustrau, *RF and Microwave Engineering, Fundamentals of Wireless Communications*. Dortmund University of Applied Sciences and Arts, 2. ed., 2012.

[32] D. M. Pozar, *Microwave Engineering*. John Wiley & Sons, Inc., 4. ed., 2005.

[33] C. Abert, *Seminar on Micromagnetics and Spintronics: Models and Simulation*, 2023.

[34] COMSOL Inc., *RF Module User's Guide v5.3*, 2017.

[35] "Coplanar waveguide analysis/synthesis calculator." `https://wcalc.sourceforge.net/cgi-bin/coplanar.cgi`. Accessed: 2023-12-28.

[36] G. Rosenblatt, B. Simkhovich, G. Bartal, and M. Orenstein, "Nonmodal plasmonics: Controlling the forced optical response of nanostructures," *Physical Reviex X*, vol. 10, p. 011071, 2020.

[37] T. Tsutaoka, T. Kasagi, and K. Hatakeyama, "Permeability spectra of yttrium iron garnet and its granular composite materials under dc magnetic field," *Journal of Applied Physics*, vol. 110, p. 053909, 2011.

[38] E. Hartmann, L. Kovács, and J. Paitz, "Electrical conductivity of gadolinium–gallium garnet (ggg) crystals," *Physica Status Solidi (a)*, vol. 86, pp. 401–405, 1984.

[39] S. Klingler, A. Chumak, T. Mewes, B. Khodadadi, C. Mewes, C. Dubs, O. Surzhenko, B. Hillebrands, and A. Conca, "Measurements of the exchange stiffness of yig films by microwave resonance techniques," *Journal of Physics D Applied Physics*, vol. 48, p. 015001, 2014.

[40] R. O. Serha, A. A. Voronov, D. Schmoll, R. Verba, K. O. Levchenko, S. Koraltan, K. Davídková, B. Budinska, Q. Wang, O. V. Dobrovolskiy, M. Urbánek, M. Lindner, T. Reimann, C. Dubs, C. Gonzalez-Ballestero, C. Abert, D. Suess, D. A. Bozhko, S. Knauer, and A. V. Chumak, "Magnetic anisotropy and ggg substrate stray field in yig films down to millikelvin temperatures," *arXiv:2402.12112v1 [cond-mat.mes-hall]*, 2024.

[41] D. A. Connelly, H. R. O. Aquino, M. Robbins, G. H. Bernstein, A. Orlov, W. Porod, and J. Chisum, "Complex permittivity of gadolinium gallium garnet from 8.2 to 12.4 ghz," *IEEE Magnetics Letters*, vol. 12, pp. 1–4, 2021.

[42] A. Siblini, I. Khalil, J. P. Chatelon, and J. J. Rousseau, "Determination of initial magnetic permeability of yig thin films using the current sheet method," *Advanced Materials Research*, vol. 324, pp. 290–293, 2011.

[43] F. Bruckner, S. Koraltan, C. Abert, and D. Suess, "magnum.np: a pytorch based gpu enhanced finite difference micromagnetic simulation framework for high level development and inverse design," *Scientific Reports*, vol. 13, p. 12054, 2023.

[44] L. Körber, G. Quasebarth, A. Otto, and A. Kákay, "Finite-element dynamic-matrix approach for spin-wave dispersions in magnonic waveguides with arbitrary cross section," *AIP Advances*, vol. 11, p. 095006, 2021.

[45] H. Qin, S. J. Hämäläinen, K. Arjas, J. Witteveen, and S. van Dijken, "Propagating spin waves in nanometer-thick yttrium iron garnet films: Dependence on wave vector, magnetic field strength, and angle," *Physical Review B*, vol. 98, p. 224422, 2018.

[46] J. P. Dehollain, J. J. Pla, E. Siew, K. Y. Tan, A. S. Dzurak, and A. Morello, "Nanoscale broadband transmission lines for spin qubit control," *Nanotechnology*, vol. 24, p. 015202, 2012.

[47] T. Groves, "3 - electron beam lithography," in *Nanolithography* (M. Feldman, ed.), pp. 80–115, Woodhead Publishing, 2014.

[48] "Raith gmbh." `https://raith.com/product/raith150-two/`. Accessed: 2024-01-08.

[49] J. Zhang, M. Fouad, M. Yavuz, and B. Cui, "Charging effect reduction in electron beam lithography with nA beam current," *Microelectronic Engineering*, vol. 88, pp. 2196–2199, 2011.

[50] L. Ren and B. Chen, "Proximity effect in electron beam lithography," *Journal of Vacuum Science and Technology*, vol. 12, pp. 579 – 582 vol.1, 2004.

[51] Y. Takahashi, "Two hundred years of lichtenberg figures," *Journal of Electrostatics*, vol. 6, pp. 1–13, 1979.

[52] P. R. Emtage, "Interaction of magnetostatic waves with a current," *Journal of Applied Physics*, vol. 49, pp. 4475–4484, 1978.

[53] B. A. Kalinikos and A. N. Slavin, "Theory of dipole-exchange spin wave spectrum for ferromagnetic films with mixed exchange boundary conditions," *Journal of Physics C: Solid State Physics*, vol. 19, p. 7013, 1986.

[54] P. Hansen, P. Röschmann, and W. Tolksdorf, "Saturation magnetization of gallium-substituted yttrium iron garnet," *Journal of Applied Physics*, vol. 45, pp. 2728–2732, 1974.

A Sample inspection

In the following Figures microscope images of the fabricated structures are shown. In Figure 47 three out of four CPW antennas are shown. In Figure 48, 49 and 50, images of the 50 Ω, 100 Ω and single stripline antennas are shown respectively.

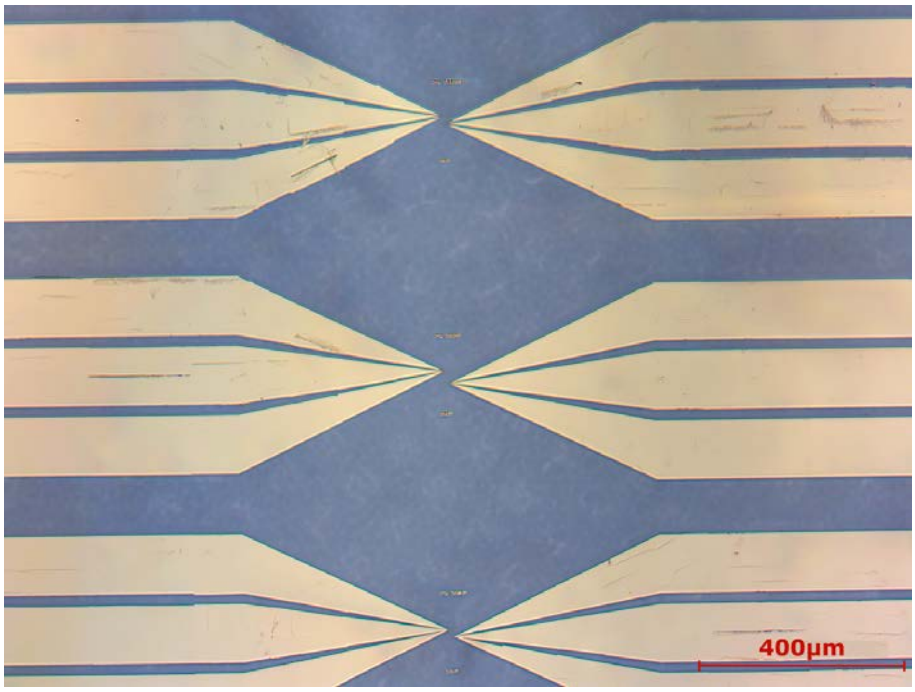

Figure 47: Microscopy image of three out of four CPW antennas.

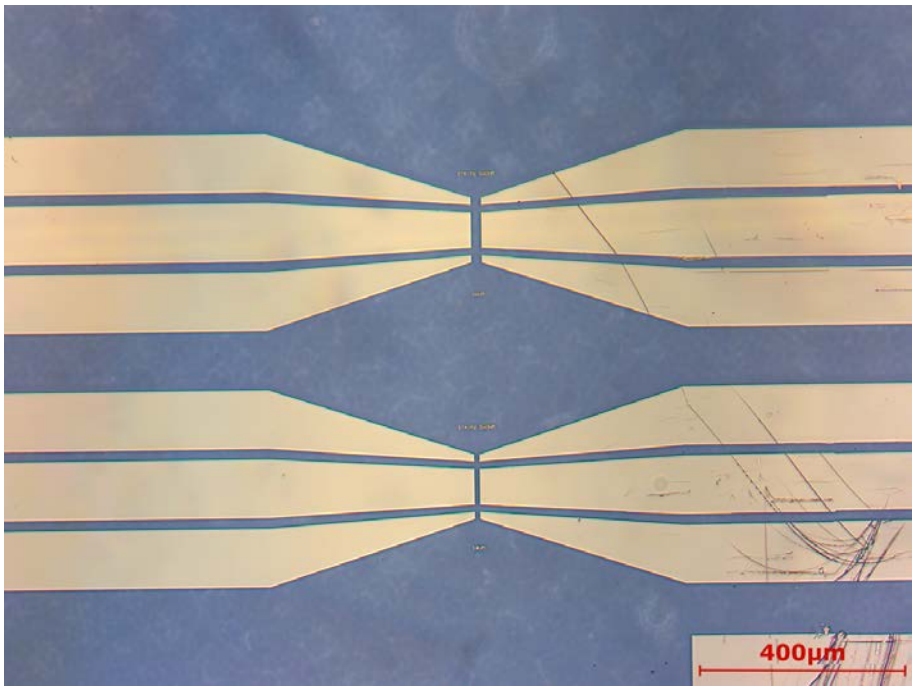

Figure 48: Microscopy image of the 50 Ω stripline antennas.

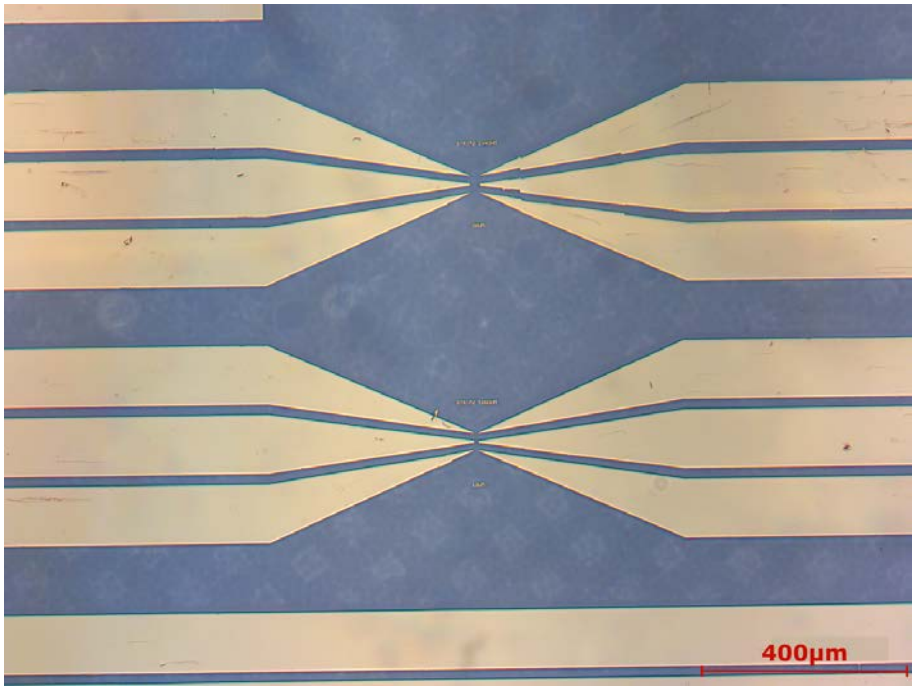

Figure 49: Microscopy image of the 100 Ω stripline antennas.

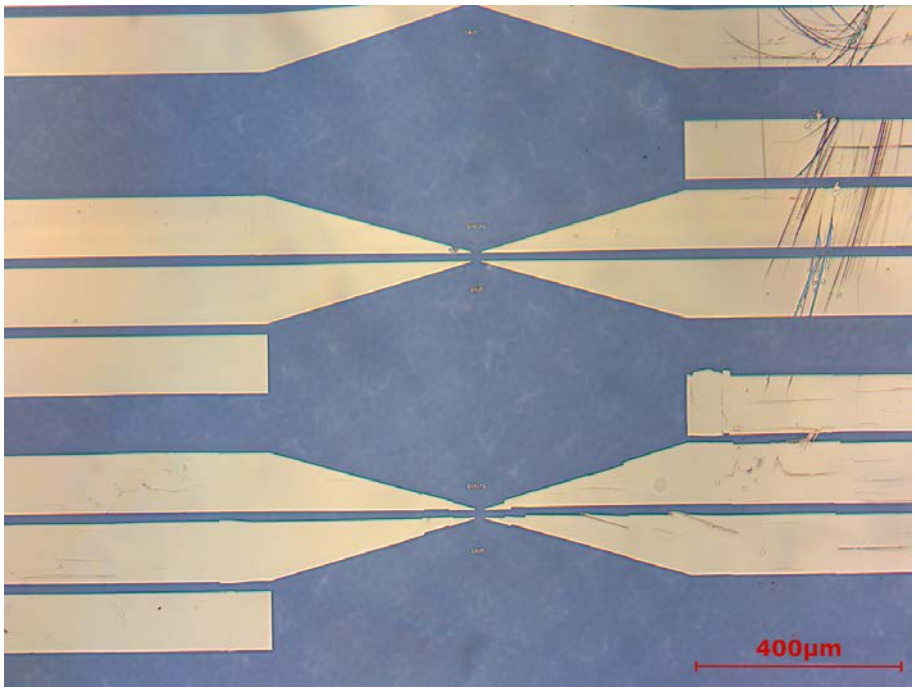

Figure 50: Microscopy image of the single stripline antennas.

B AEPSWS

The magnitude, $\mathrm{Mag}(S_{21}) = \sqrt{\mathrm{Im}(S_{21})^2 + \mathrm{Re}(S_{21})^2}$, of the four used antennas is plotted in Figures 51, 52, 54, 55 and 56 in linear scale for static magnetic field strength of 25 mT, 75 mT, 125 mT, 225 mT and 250 mT.

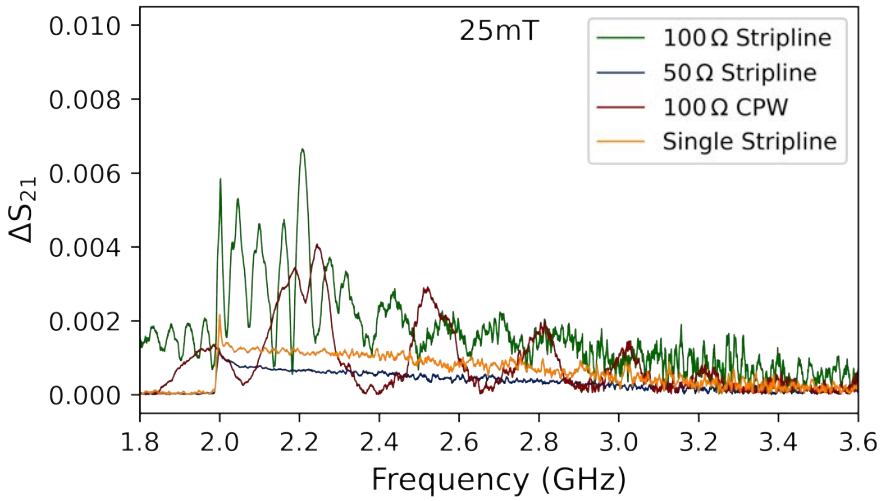

Figure 51: Magnitude of the SW transmission signal ΔS_{21}, for 100 Ω CPW, 100 Ω stripline, 50 Ω stripline and single stripline antenna, at an antenna gap of 20 µm and an applied static magnetic field of 25 mT.

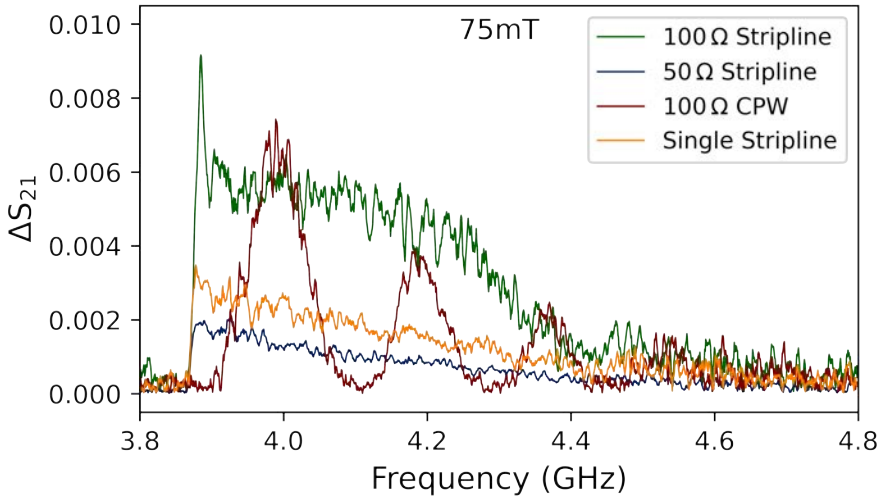

Figure 52: Magnitude of the SW transmission signal ΔS_{21}, for 100 Ω CPW, 100 Ω stripline, 50 Ω stripline and single stripline antenna, at an antenna gap of 20 µm and an applied static magnetic field of 75 mT.

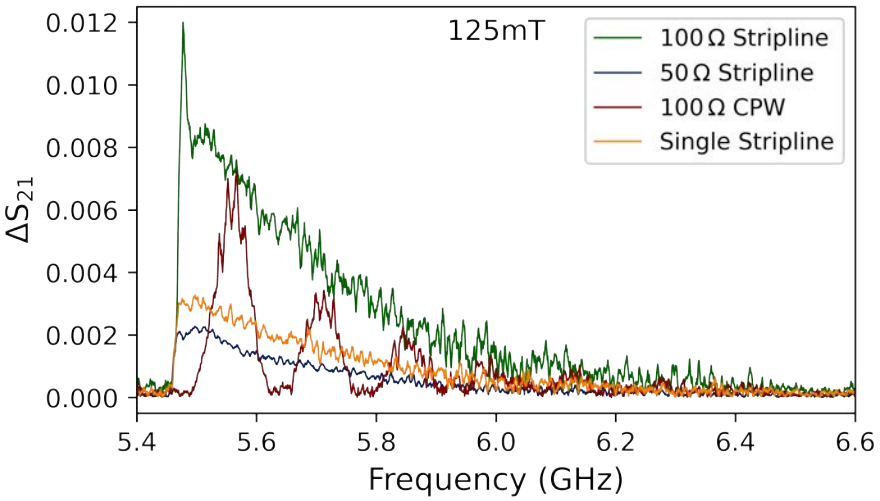

Figure 53: Magnitude of the SW transmission signal ΔS_{21}, for 100 Ω CPW, 100 Ω stripline, 50 Ω stripline and single stripline antenna, at an antenna gap of 20 µm and an applied static magnetic field of 125 mT.

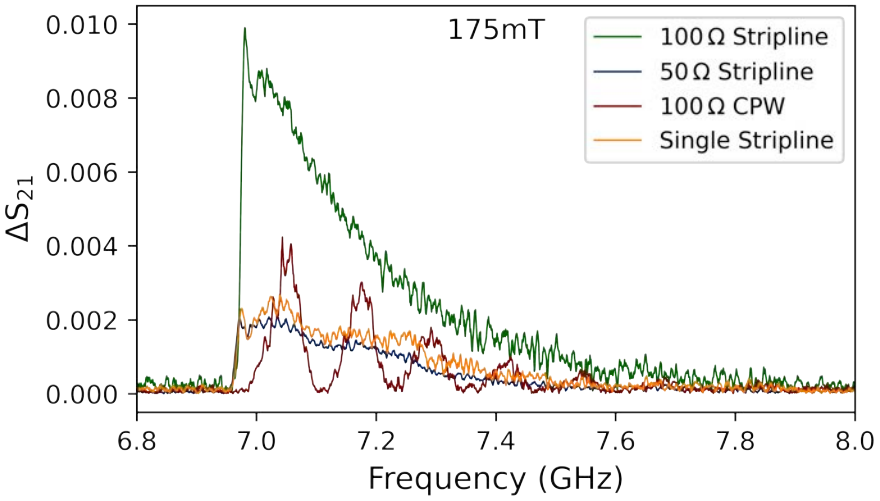

Figure 54: Magnitude of the SW transmission signal ΔS_{21}, for 100 Ω CPW, 100 Ω stripline, 50 Ω stripline and single stripline antenna, at an antenna gap of 20 µm and an applied static magnetic field of 175 mT.

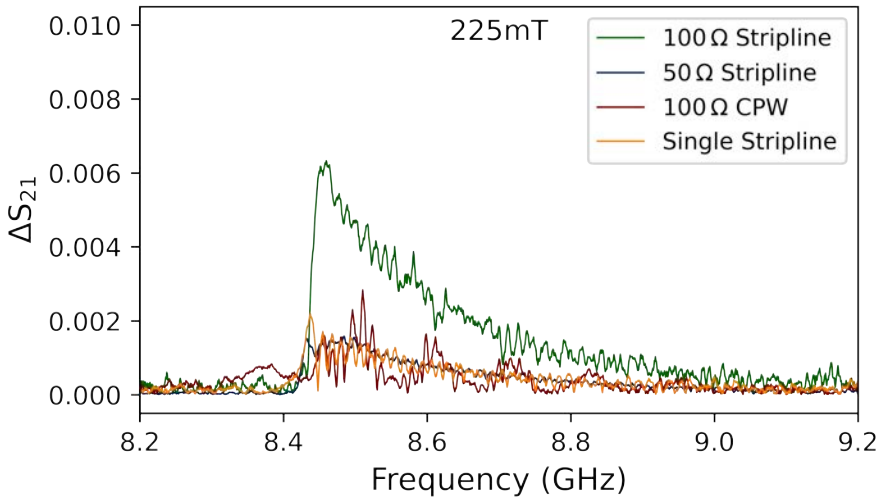

Figure 55: Magnitude of the SW transmission signal ΔS_{21}, for 100 Ω CPW, 100 Ω stripline, 50 Ω stripline and single stripline antenna, at an antenna gap of 20 µm and an applied static magnetic field of 225 mT.

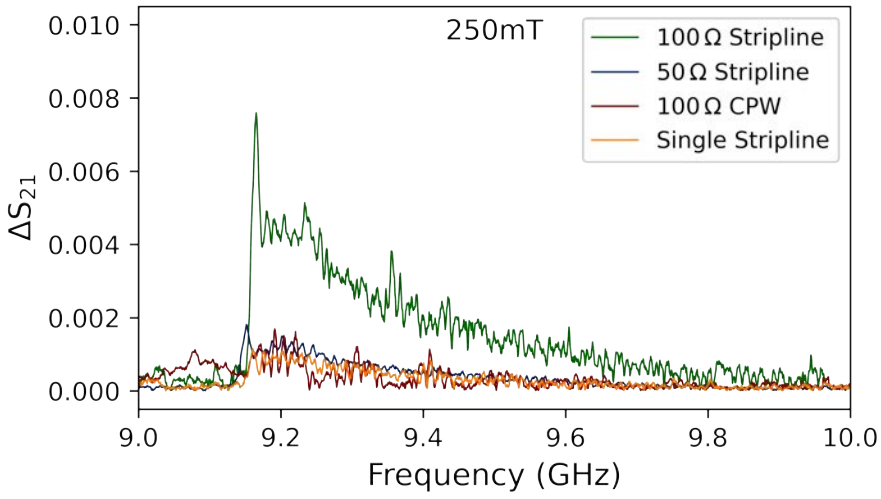

Figure 56: Magnitude of the SW transmission signal ΔS_{21}, for 100 Ω CPW, 100 Ω stripline, 50 Ω stripline and single stripline antenna, at an antenna gap of 20 µm and an applied static magnetic field of 250 mT.

List of Tables

List of Figures